ResearchGate

See discussions, stats, and author profiles for this publication at: https://www.researchgate.net/publication/304576587

Ore-fluid geochemistry and metallogeny of the Dunde iron–zinc deposit in western Tianshan, Xinjiang, China: Evidence from fluid inclusions, REE and C–O–Sr isotopes of calcite

Article *in* Ore Geology Reviews · June 2016

DOI: 10.1016/j.oregeorev.2016.06.024

CITATION
1

READS
144

5 authors, including:

Shuang Yan
Chinese Academy of Sciences
8 PUBLICATIONS **56** CITATIONS
SEE PROFILE

Jian-xin Zhao
The University of Queensland
376 PUBLICATIONS **7,861** CITATIONS
SEE PROFILE

Zhiwei Bao
Chinese Academy of Sciences
83 PUBLICATIONS **2,365** CITATIONS
SEE PROFILE

Weidong Sun
Institute of Oceanology
391 PUBLICATIONS **22,771** CITATIONS
SEE PROFILE

Some of the authors of this publication are also working on these related projects:

Cretaceous Magmatism and Associated Copper Deposits in Bahr Asman Region, South of Kerman Magmatic Belt View project

Serpentinization processes View project

All content following this page was uploaded by Shuang Yan on 15 April 2019.

The user has requested enhancement of the downloaded file.

Ore Geology Reviews 100 (2018) 441–456

Contents lists available at ScienceDirect

Ore Geology Reviews

journal homepage: www.elsevier.com/locate/oregeo

Ore-fluid geochemistry and metallogeny of the Dunde iron–zinc deposit in western Tianshan, Xinjiang, China: Evidence from fluid inclusions, REE and C–O–Sr isotopes of calcite

Shuang Yan [a,b,c], He-Cai Niu [a,b,*], Jian-xin Zhao [d], Zhi-Wei Bao [a,b], Wei-dong Sun [a,b]

[a] CAS Key Laboratory of Mineralogy and Metallogeny, Guangzhou Institute of Geochemistry, Chinese Academy of Sciences, Guangzhou 510640, China
[b] Guangdong Provincial Key Laboratory of Mineral Physics and Materials, Guangzhou 510640, China
[c] University of Chinese Academy of Sciences, Beijing 100049, China
[d] Department of Earth Sciences, University of Queensland, Brisbane, QLD, 4072, Australia

ARTICLE INFO

Article history:
Received 11 March 2016
Received in revised form 22 June 2016
Accepted 22 June 2016
Available online 27 June 2016

Keywords:
Submarine volcanic-hosted iron oxide deposits
Dunde iron–zinc deposit
Western Tianshan
Hydrothermal calcite
Ore-forming fluids
Metallogenesis

ABSTRACT

The Dunde iron–zinc deposit is a typical submarine volcanogenic iron oxide deposit in the eastern Awulale Metallogenic Belt of the western Tianshan. We report new petrography, rare earth elements (REE), and fluid inclusion microthermometry and C–O–Sr isotopes of the calcite from the skarn and the magnetite ores from the Dunde deposit. Calcite from both the skarn and magnetite ores displays high LREE/HREE (44–172), implying significant REE fractionation. We infer that the complexation of Cl (±F) during the fluid circulation and mineralogical control of calcite at the depositional sites were important for the LREE enrichment in the Dunde calcite. The restricted Y/Ho (26.7–32.1) suggests that calcite in the skarn and magnetite ores was co-genetic and the superchondritic Y/Ho may have resulted from the preferential incorporation of Y over Ho in calcite. Positive Eu anomaly (1.23–1.63) of the skarn calcite may have been inherited from the parental fluids, while the negative or slightly positive anomaly (0.65–1.04) of the magnetite ore calcite may have been resulted from the high Sr^{2+} content that suppressed Eu^{2+} in calcite.

Fluid inclusion microthermometric results exhibit a wide range of homogenization temperatures (106 °C–364 °C) and salinities (0.2 wt.%–41.5 wt.% NaCl equiv.). Three kinds of ore-forming fluids can be distinguished, i.e., high-salinity (>35 wt.% NaCl equiv.), medium-salinity (10 wt.%–35 wt.% NaCl equiv.) and low-salinity (<10 wt.% NaCl equiv.) fluids. The high-salinity fluid was likely to be magma-derived and occurred in both the skarn- and magnetite ore calcite. The low-salinity fluid, possibly seawater-derived, was found only in the skarn calcite. The medium-salinity fluid, mainly of $CaCl_2$–H_2O aqueous- and brine-featured fluids, may have been the product of the fluid–rock interactions as the magmatic fluids and seawater circulated through the strata. The Dunde calcite has $\delta^{13}C$ comparable to marine carbonates, but $\delta^{18}O$ substantially lower, suggesting possibly a result of limestone dissolution. Calculated $\delta^{18}O$ of the fluids in equilibrium with calcite vary from −0.78‰ to 5.46‰ (−0.78‰–1.85‰ and 2.15‰–5.46‰ for skarn calcite and magnetite ore calcite, respectively), implying magmatic fluids and seawater mixing. The Dunde calcite $^{87}Sr/^{86}Sr$ (0.7071 to 0.7078) correlate positively with 1/Sr, implying that two sources, i.e., basaltic/andesitic volcanic wall rocks ($^{87}Sr/^{86}Sr$: 0.7056–0.7066) and limestones/seawater ($^{87}Sr/^{86}Sr$: 0.7075–0.7089), may have been involved in the mineralization. Mass-balance calculation between fresh basaltic tuff and its neighboring skarn showed that extra Ca, Mg and Fe were added to the basaltic tuff during the hydrothermal alteration. The limestone dissolution during the fluid–rock interactions may have added Ca to the ore-forming fluids, while Fe and Mg may have been introduced from the deep-seated magmatic system via the heated Cl-rich fluid circulation.

© 2016 Elsevier B.V. All rights reserved.

1. Introduction

The Chinese Submarine volcanic-hosted iron oxide (SVIO) deposits are unique in the world and distinct from the SVIO ones defined by Dill (2010). They are among the most important sources

* Corresponding author at: CAS Key Laboratory of Mineralogy and Metallogeny, Guangzhou Institute of Geochemistry, Chinese Academy of Sciences, Guangzhou 510640, China.
E-mail address: niuhc@gig.ac.cn (H.-C. Niu).

https://doi.org/10.1016/j.oregeorev.2016.06.024
0169-1368/© 2016 Elsevier B.V. All rights reserved.

of high-grade iron ores in China (Jiang and Wang, 2005; Hu et al., 2011, 2014a) and developed in various tectonic settings including arc, back-arc, rift and mid-ocean ridge environments with a wide range of formation ages from Paleoproterozoic to Mesozoic (Hou et al., 2014a; Zhang et al., 2014b; Li et al., 2015a). Most of the Chinese SVIO deposits are characterized by extensive skarn alteration. However, the skarn lacks a close relationship with any intrusive rocks in time and space (e.g., Xu et al., 2010; Zhao and Zhou, 2011; Hong et al., 2012; Zhang et al., 2012b), leading to debates on its genesis. Some workers proposed that the skarn was developed by the interactions between the buried intrusion-derived fluids and volcanic wall rocks (e.g., Meinert et al., 2005; Duan et al., 2014), whereas others suggested that it was resulted from the interactions between the basaltic/andesitic magma and the limestone (e.g., Ge et al., 2014; Hou et al., 2014b; Li et al., 2014; Sun et al., 2015). Consequently, various models were proposed for the their metallogenesis, including silicate liquid immiscibility (e.g., Feng et al., 2010; Wang et al., 2011; Zhang et al., 2014), submarine volcanic exhalative syn-sedimentation (e.g., Wang et al., 2001; Yuan, 2003), intrusion-related skarn (e.g., Zhang et al., 2012b; Duan et al., 2014) and volcanic-related skarn (e.g., Ge et al., 2014; Hou et al., 2014b; Sun et al., 2015).

The Awulale Metallogenic Belt (AMB) in the western Tianshan is one of the most important Chinese SVIO deposit belts (Hou et al., 2014a; Zhang et al., 2014b; Li et al., 2015a; Sun et al., 2015), in which several medium-to-large scale iron deposits including Chagangnuoer, Zhibo, Dunde, Beizhan, and Wuling, were discovered. These iron deposits possess a total iron ore reserve of over 1.2 billion tons, of which some 30 wt.% are high grade ores (Fe content >50 wt.%). All these iron deposits are hosted in the Late Carboniferous Dahalajunshan Formation submarine volcanic/volcanoclastic successions and characterized by well-developed skarn (e.g., Zhang et al., 2012b; Duan et al., 2014; Jiang et al., 2014; Zhang et al., 2014; Yan et al., 2015). A substantial number of petrologic, geochemical and geochronological studies have been conducted on the iron deposits in the AMB, constraining their formation in a nascent-back-arc environment during the Late Carboniferous (e.g., Hong et al., 2012; Duan et al., 2014; Jiang et al., 2014; Li et al., 2015b; Yan et al., 2015).

The Dunde iron–zinc deposit is a typical example of the SVIO deposit in the AMB. The iron orebodies at Dunde are spatially related to the skarn. To establish the relationship between the skarn alteration and iron mineralization at Dunde, the interstitial calcite in the skarn and the cloddy calcite in the magnetite ores were investigated. Calcite records the ore-forming fluid geochemistry (e.g., Webb and Kamber, 2000; Munemoto et al., 2015; Zaky et al., 2015; Debruyne et al., 2016) that can be excellent tracers for the fluid sources and evolution (e.g., Kontak and Kerrich, 1997; Hecht et al., 1999; Chen et al., 2011; Shen et al., 2011; Wang et al., 2015). On the basis of petrographic observation, fluid inclusion (FI) microthermometry, REE and C–O–Sr isotopes of the Dunde calcite, we discuss the calcite genesis and the possible sources and evolution of the ore-forming fluids to shed light on the metallogenesis of the Chinese SVIO deposits.

2. Regional geology

The E–W-trending AMB is part of the Central Asia Orogenic Belt (Fig. 1a), and lies within the Yili-Central Tianshan Block (YCTB). The AMB has a Mesoproterozoic metamorphic basement, consisting mainly of marble, biotite-plagioclase gneiss and hornblende-plagioclase gneiss (Gao et al., 1998; Li et al., 2009a; Feng et al., 2010). The basement is covered by sequences of the Silurian to Jurassic carbonate-volcanic rocks, marine volcanic/volcanoclastic rocks and terrigenous clastic-carbonate rocks (Hu et al., 2000; Li et al., 2009b; Liu et al., 2014; Wang et al., 2014). The Silurian and Devonian volcanoclastic rocks are exposed along the northern- and southern margins of the AMB, while coeval limestones are widespread in the eastern AMB (Feng et al., 2010). The Carboniferous volcanic/volcanoclastic rocks are mostly distributed in the eastern AMB, while the Permian continental clastic rocks and post-collisional volcanic rocks mainly occur in the western AMB (e.g., Wang et al., 1990; Allen et al., 1993). During the Late Paleozoic, the YCTB had experienced the South Tianshan Ocean subduction from the south and the North Tianshan Ocean subduction from the north (Wang et al., 2008; Gao et al., 2009a; Xiao et al., 2013), which both ceased at the end of Late Carboniferous (Chen et al., 1999; Gao et al., 2009a,b; Xiao et al., 2013) and led to the amalgamation of the Tarim Plate, Junggar Plate and the YCTB (Bazhenov et al., 2003; Wang et al., 2007; Tang et al., 2014).

Along the AMB, the Fe deposits, including Songhu, Shikebutai, Chagangnuoer, Zhibo, Dunde and Beizhan, are distributed in the middle and eastern part and hosted in the Carboniferous volcanic/volcanoclastic rocks while the Cu deposits, e.g., Qunjisayi, Qiongbulake, Chuangjisayi and Mosizaote, etc., cluster in the western part and are hosted in the Permian volcanic rocks (Fig. 1b). Major structures in the AMB include E–W-trending (steeply north-dipping) faults and a syncline. Remote sensing images show a caldera structure in the eastern AMB. The Zhibo iron deposit is situated at the caldera center while the Dunde, Wuling, Chagangnuoer and Beizhan iron deposits are distributed along the radiating caldera faults (Fig. 1c).

3. Ore deposit geology and petrography

The Dunde iron–zinc deposit is a large iron deposit in the eastern AMB with a proven reserve of 185 Mt iron ore @35.06% and 1.49 Mt zinc ore @1.26% (Duan et al., 2014). The deposit lies about 10 km to the southeast of the crater center. Currently, seven orebodies have been discovered, among which three in the west are outcropped and four in the east are buried. The four orebodies in the east contribute most of the iron resource and are more prospective for further exploration. The stratiform, plate-like and lenticular orebodies are hosted in the Late Carboniferous Dahalajunshan Formation grayish-green basaltic tuff and purplish-red andesite. Wall rock alteration is locally intensive, forming alteration minerals such as chlorite, epidote and actinolite (referring to the geological report by #3 Brigade of the Xinjiang Bureau of Geology and Mineral Resources). Intrusive rocks, including alkali feldspar granite and a few diabase, intrude into the volcanic rocks at southwestern Dunde (Fig. 2a). As observed in the Tunnel 3788, skarn occurs along the contact between the basaltic-andesitic volcanic rocks and limestones (Fig. 2b). The basaltic tuff is of tuffaceous texture and massive structure and contains crystal pyroclasts, vitric pyroclasts and volcanic ash, with the former comprising plagioclase (35 vol.%) and minor pyroxene (5 vol.%). The fresh andesite has a porphyritic texture and massive structure. However, most andesite in the tunnel was intensively altered and displays secondary colors, like grayish-white and light brown, etc. Only relics of plagioclase phenocrysts were identified and its groundmass mainly is made up of microcrystalline plagioclase, magnetite and chlorite (Ge, 2013). The iron orebodies occur inside or adjacent the skarn, implying close genetic relation. The deposit has this succession of superposed zones of alteration concentrically from orebody outwards: diopside, epidote, chlorite and carbonate.

Hydrothermal calcite is widespread at Dunde deposit, and that occurs in the skarn and massive magnetite ores were studied here. The skarn (Fig. 3a) is made up of diopside (~70 vol.%), garnet

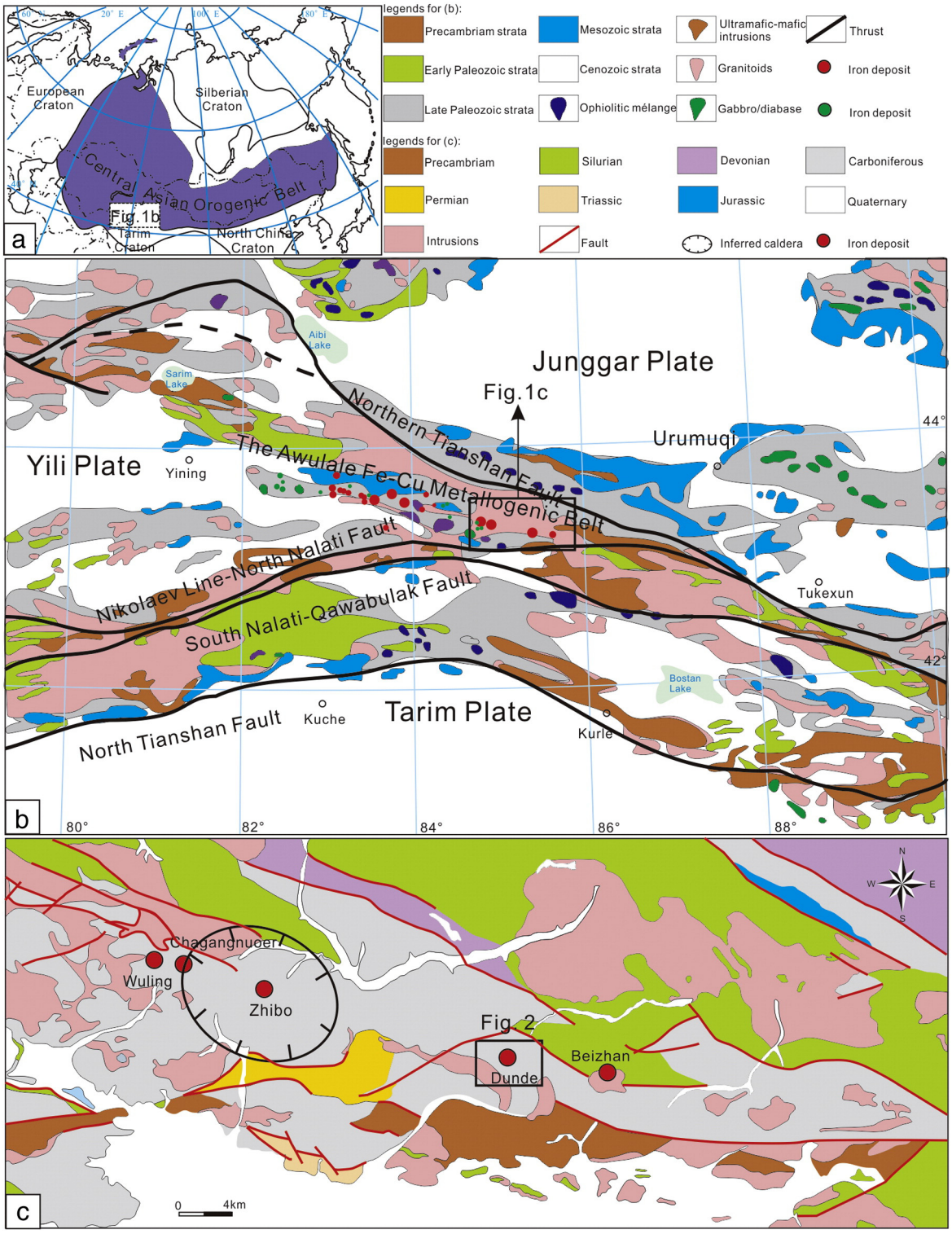

Fig. 1. (a) Tectonic map of the Central Asia Orogenic Belt and the location of the Tianshan orogen (modified from Sengör et al., 1993); (b) Geological map of the western Tianshan (NW China), showing the locations of major Fe and Cu deposits in the Awulale Metallogenic Belt (modified from Yang et al., 2012); (c) Geological map of the eastern segment of the Awulale Metallogenic Belt, showing the location of the Dunde iron–zinc deposit (modified from Zhang et al., 2012a).

(~15 vol.%), calcite (~10 vol.%) and minor magnetite (~5 vol.%). Under the microscope, the calcite occurs as interstitial minerals among garnet and diopside (Fig. 3c). In the massive magnetite ores, euhedral calcite occurs as fragments among coarse, subhedral to euhedral magnetite grains (Fig. 3b). Calcite fragments range from several to a dozen centimeters in size and show straight boundaries with the magnetite grains (Fig. 3d). No replacement texture has been observed along the boundary (Fig. 3d), suggesting the magnetite grains and calcite fragments may have precipitated from the same fluid.

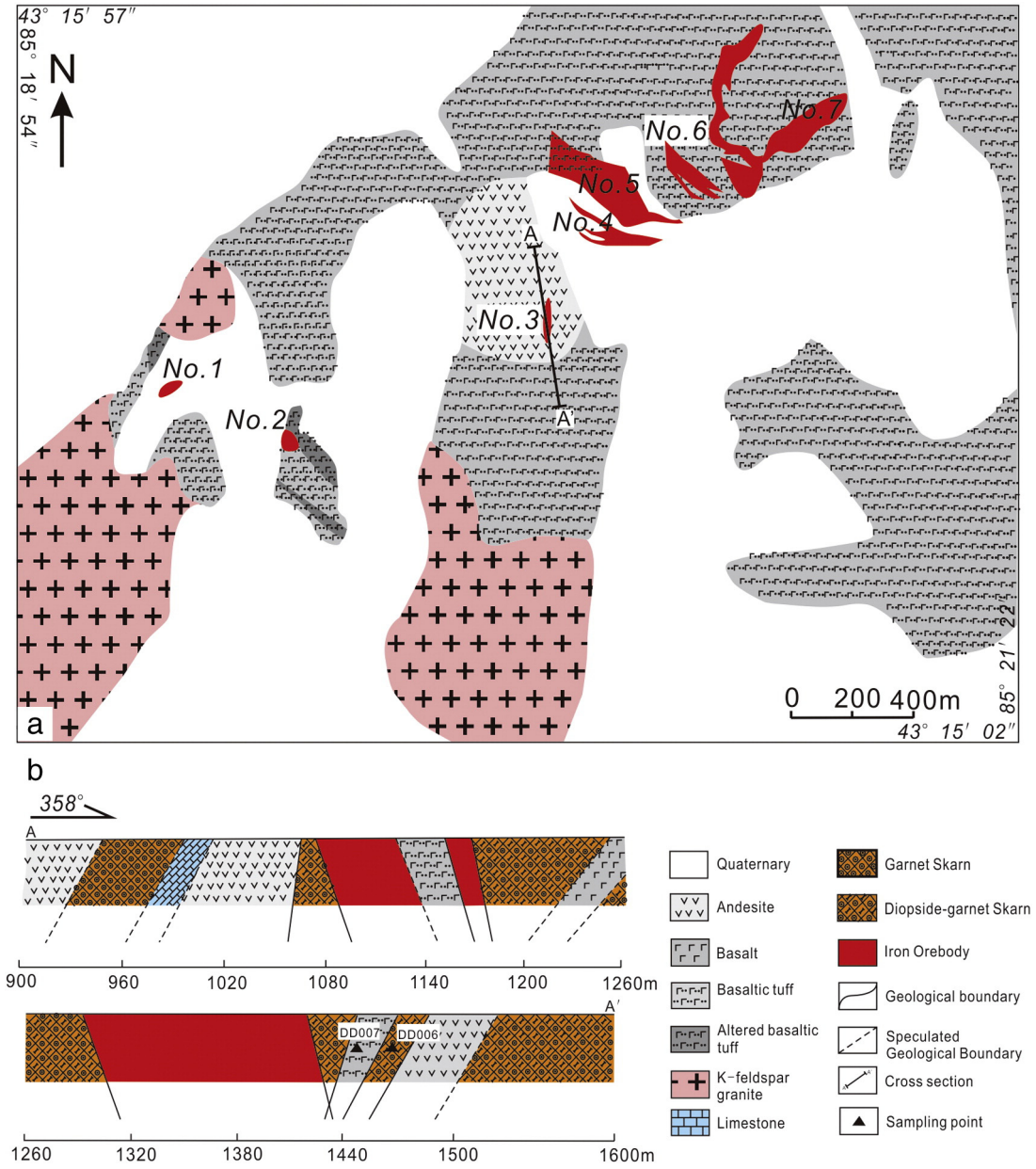

Fig. 2. (a) Geological map of the Dunde iron–zinc deposit (modified after Ge, 2013); (b) Orebody cross-sections at the depth of 3788 m in the Dunde iron–zinc deposit (modified after Ge, 2013).

4. Sampling and analytical methods

Six skarn samples (13DD-3, 13DD-4, 13DD-6, 13DD-7, 13DD-8 and 13DD-9) and 12 magnetite ore samples (13DD-21, 13DD-22, 13DD-23, 13DD-24, 13DD-32 and DD-1 to DD-7) were collected from the skarn zone and magnetite ore zone in Tunnel 3788, respectively. Calcite in the garnet-diopside skarn and massive magnetite ores were checked using 2% HCl solution to ensure their pureness before analyses. First, dozens of double-polished thin sections containing calcite (0.3 mm thick) were prepared for the microthermometry. Fresh calcite was hand-picked and then crushed into grains of millimeter level. Impurities were removed under the binocular microscope after washing with distilled water for several times and drying over hotplate at 105 °C. Finally, the pure calcite particles were grinded into 200 mesh for analyses. Analyses of trace elements, carbon and oxygen stable isotopes and fluid inclusions of the calcite were carried out at the Guangzhou Institute of Geochemistry, Chinese Academy of Sciences, while Sr isotope analysis was carried out at the Department of Earth Sciences, University of Queensland (Australia).

4.1. Trace element geochemical analysis of calcite

About 45 mg powder of each calcite sample was dissolved in a Teflon bomb with 1 ml of HF (38%) and 0.5 ml of HNO_3 (68%). The sealed bomb was heated to 190 °C and kept for 48 h. 1 ml of 1 lg/ml Rh was added to the cooled solution as the internal standard and the solution was then evaporated. 1 ml of HNO_3 (68%) was added, evaporated to dryness and the process repeated twice. The final residue was retrieved by 8 ml of HNO_3 (40%). The bomb was sealed and heated to 110 °C for 3 h. The final solution was diluted to

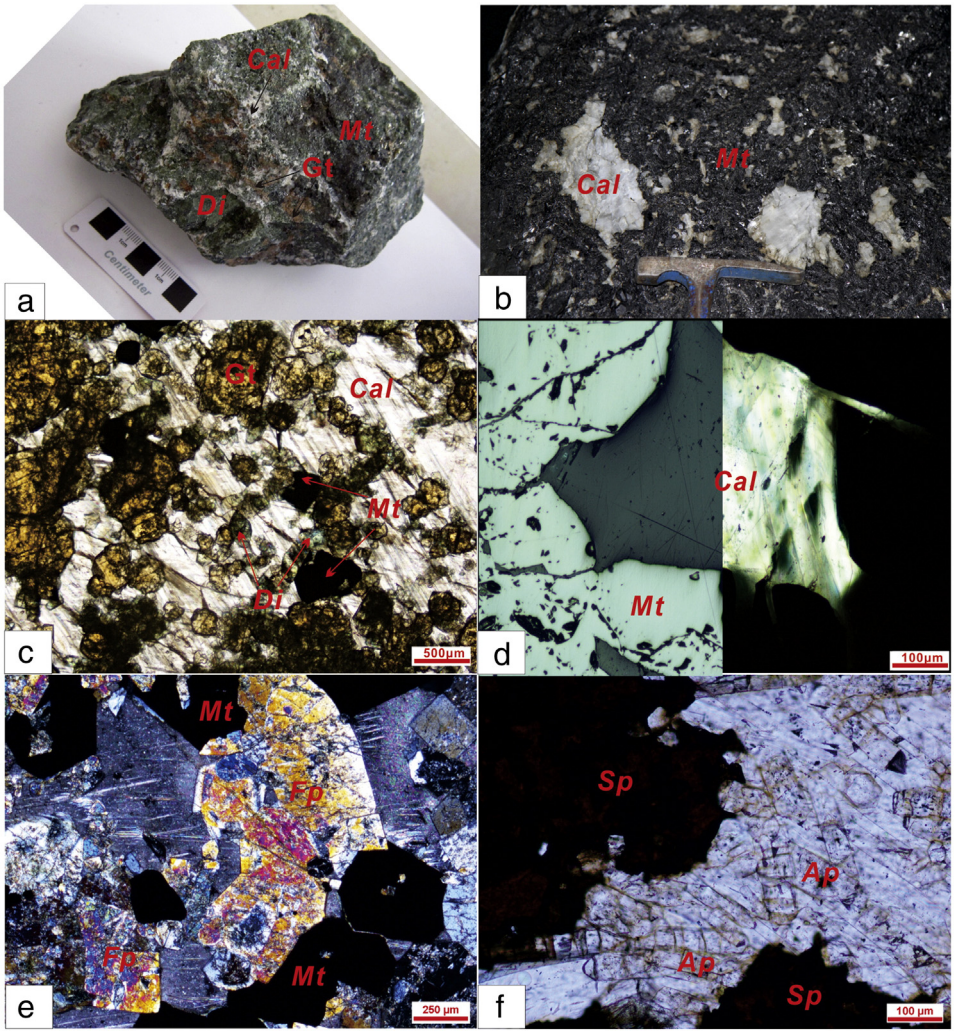

Fig. 3. (a) Hand specimen of intergranular calcite in the skarn; (b) hand specimen of cloddy calcite in the massive magnetite ore; (c) photomicrograph of the textural relationships between calcite and skarn minerals; (d) photomicrograph of the paragenesis between calcite and magnetite; (e) photomicrograph of euhedral ferropargasite; (f) photomicrograph of euhedral apatite and sphalerite replaces apatite. Abbreviation: Cal = calcite, Gt = garnet, Di = diopside, Mt = magnetite, Fp = ferropargasite, Ap = apatite, Sp = sphalerite.

100 ml by adding distilled deionized water for the ICPMS analysis. Precision of analytical results as estimated from replicate measurements was better than 10% RSD. Details of this procedure are given in Li (1997).

4.2. C–O–Sr isotope analyses of calcite

Analyses of carbon and oxygen stable isotopes were carried out with a VG IsoPrime II mass spectrometer. The samples (ca. 20 mg) were reacted with 100% H_3PO_4 in a vacuum at 25 °C. The CO_2 liberated was analyzed for carbon and oxygen isotopes. Analytical uncertainties are better than ±0.05% for $\delta^{13}C$ (relative to V-PDB standard) and ±0.08% for $\delta^{18}O$ (relative to SMOW standard). For Sr isotope determination, about 80 mg of calcite powders were first dissolved in Teflon capsules with ($HF + HNO_3$) acid. Secondly, Sr and REE were separated using cation exchange resin columns. Strontium isotopic compositions were analyzed on the thermal ionization mass spectrometry (TIMS), following procedures described in Uysal et al. (2007). Measured $^{87}Sr/^{86}Sr$ was normalized to $^{86}Sr/^{88}Sr = 0.1194$ and the reported $^{87}Sr/^{86}Sr$ was adjusted to the NBS SRM 987 standard $^{87}Sr/^{86}Sr = 0.71025$.

4.3. Fluid inclusion analyses

Types of fluid inclusions (FIs) were identified under the microscope based on the petrographic observation and representative thin sections were selected for microthermometric study. Microthermometry experiment was carried out on a Linkam MDS 600 Heating–Freezing System at the Key Laboratory of Mineralogy and Metallogeny, Chinese Academy of Sciences. The accuracy of the measurements was ensured by calibration with the triple point of synthetic CO_2–H_2O (−56.6 °C), and the freezing point of pure water FIs (0 °C) before testing our samples. The precision of temperature measurement is ±0.1 °C for −100 °C–25 °C, ±1 °C for 25 °C–400 °C, and ±2 °C for above 400 °C. The heating/freezing rate was generally 0.5–20 °C/min during the FI testing process, but reduced to 0.1 °C/min near the freezing point and 0.2 °C/min near the homogenization temperature to capture the phase transformation process. Apparent salinities for FIs are expressed as weight percent NaCl equivalent (wt.% NaCl equiv.) and calculated from the final ice melting temperature (Bodnar, 1994). For daughter-mineral-bearing FIs, salinities are also expressed as wt.% NaCl equiv. and calculated using the final melting temperatures of hydrohalite (Lecumberri-Sanchez et al., 2012).

5. Results

5.1. Rare earth elements of calcite

The rare earth element (REE) concentrations of calcite are presented in Table 1. As shown in the Figs. 4 and 5, the calcite from the skarn (termed C1 hereafter) has high REE contents (71–183 ppm), high LREE/HREE (58–172) and significant positive Eu anomalies (1.23–1.63), with Y/Ho and La/Ho being 26.7 to 31.5 and 450 to 1791, respectively; in contrast, the calcite from the magnetite ores (termed C2 hereafter) has lower REE contents (42–71 ppm), lower LREE/HREE (44–77), and slightly positive or even negative Eu anomalies (0.65–1.04), with Y/Ho and La/Ho being 27.5 to 32.1 and 418 to 915, respectively.

5.2. C–O–Sr isotopes of calcite

The calcite carbon- and oxygen isotopic compositions are listed in Table 2 and plotted in Fig. 9. C1 is characterized by a narrow $\delta^{13}C$ range (0.05‰ to 0.47‰; 0.25‰ on average) and relatively wide $\delta^{18}O$ range (9.22‰ to 11.85‰; 10.68‰ on average). Both $\delta^{13}C$ and $\delta^{18}O$ of C2 are slightly higher than those of C1, being 0.21‰ to 0.86‰ (0.63‰ on average) and 13.33‰ to 15.22‰ (14.15‰ on average), respectively. $\delta^{18}O$ of the fluids in equilibrium with calcite was calculated based on the average FI homogenization temperatures, and the calcite-water oxygen isotope equilibrium fractionation factors proposed by Zheng (1999). The fluids in equilibrium with C1 have $\delta^{18}O$ of −0.78‰ to 1.85‰ (0.68‰ on average), whereas the fluids in equilibrium with C2 have $\delta^{18}O$ of 2.15‰ to 5.46‰ (3.2‰ on average) (Table 2).

Calcite Sr-isotope data are listed in Table 3 plotted in Fig. 10. C1 has Rb and Sr concentrations of 0.1 ppm to 0.42 ppm and 164 ppm to 201 ppm, respectively. Compared with C1, C2 has lower Rb and higher Sr concentrations of 0.05 ppm to 0.1 ppm and 181 ppm to 270 ppm, respectively. Both C1 and C2 are characterized by extremely low Rb/Sr (0.0005–0.0023 and 0.0002–0.0004). C1 has Sr isotope of 0.707198 to 0.707790, while C2 has slightly lower Sr isotope of 0.707148 to 0.707345.

5.3. Fluid inclusion petrography and microthermometry

Four types of FIs were defined in calcite at room temperature (25 °C), i.e., pure vapor and vapor-rich inclusions (V-type), liquid-rich inclusions (L-type), pure liquid inclusion (PL-type) and daughter mineral-bearing inclusions (S-type) (Fig. 6). Only the isolated or clustered FIs in calcite were selected for the microthermometric analyses. V-type FIs have high homogenization temperatures (>400 °C), and some even cannot homogenize at temperatures near

Table 1
Trace element compositions (ppm) of the calcites from the Dunde iron–zinc deposit. Note that, bdl means below detection limit.

Description	Calcite in skarn						Calcite in magnetite ore				
Sample	13DD-3	13DD-4	13DD-6	13DD-7	13DD-8	13DD-9	13DD-21	13DD-22	13DD-23	13DD-24	13DD-32
Sc	0.93	1.03	0.99	1.91	1.10	0.75	0.81	0.81	0.79	0.79	0.50
Ti	39.16	66.82	83.24	237.90	63.56	15.71	2.33	1.42	0.74	0.51	0.63
V	2.23	2.40	2.76	5.92	3.20	1.87	0.69	0.66	0.50	0.66	0.53
Cr	19.97	2.75	20.50	6.96	2.17	1.19	6.13	10.48	6.68	9.34	2.46
Co	1.45	1.93	2.00	3.81	1.55	3.01	1.32	1.61	439.80	1.42	3.55
Ni	13.4	13.4	13.6	14.8	13.6	16.3	14.0	15.0	36.6	15.5	11.6
Cu	2.56	2.21	7.94	27.2	4.03	3.41	0.68	0.44	0.77	0.41	0.33
Zn	10.9	26.5	19.0	22.6	14.3	10.0	23.7	20.2	30.7	18.4	25.2
Ga	0.36	0.37	0.41	1.19	0.42	0.25	0.14	0.11	0.12	0.13	0.08
Ge	0.27	0.23	0.26	0.62	0.28	0.18	0.14	0.07	0.11	0.09	0.06
Rb	0.42	0.16	0.39	0.25	0.12	0.10	0.05	0.07	0.06	0.05	0.10
Sr	201	182	170	164	197	191	255	181	238	268	270
Y	1.71	1.31	1.06	3.80	1.36	0.54	2.00	0.82	0.83	1.70	0.61
Zr	3.54	5.93	4.01	14.25	4.48	1.66	0.06	0.06	0.03	0.10	0.15
Nb	0.10	0.12	0.26	0.49	0.13	0.06	0.04	0.02	0.05	0.01	0.01
Cs	0.05	0.07	0.06	0.06	0.06	0.06	0.03	0.04	0.04	0.02	0.02
Ba	1.65	1.35	1.29	2.26	1.35	1.32	0.64	0.86	1.76	0.62	0.97
La	33.90	26.69	25.88	63.88	32.38	30.44	27.14	21.30	25.63	28.41	19.15
Ce	42.11	33.43	33.63	87.97	40.77	37.37	32.14	23.01	27.59	32.22	17.18
Pr	3.26	2.48	2.69	6.89	3.13	2.75	2.27	1.54	1.66	2.11	1.22
Nd	8.16	6.31	7.35	18.57	8.20	6.54	6.25	3.92	4.16	5.57	3.00
Sm	0.64	0.62	0.70	1.84	0.72	0.38	0.79	0.45	0.43	0.62	0.31
Eu	0.22	0.28	0.28	0.75	0.28	0.14	0.17	0.11	0.12	0.16	0.11
Gd	0.47	0.55	0.41	1.20	0.51	0.21	0.78	0.43	0.43	0.63	0.34
Tb	0.06	0.05	0.05	0.15	0.06	0.02	0.08	0.04	0.03	0.06	0.03
Dy	0.27	0.26	0.21	0.73	0.26	0.09	0.38	0.17	0.16	0.29	0.12
Ho	0.06	0.05	0.04	0.14	0.05	0.02	0.07	0.03	0.03	0.05	0.02
Er	0.16	0.13	0.09	0.39	0.13	0.05	0.14	0.06	0.06	0.12	0.05
Tm	0.02	0.02	0.01	0.06	0.02	0.01	0.02	0.01	0.01	0.01	0.01
Yb	0.15	0.11	0.09	0.37	0.11	0.05	0.09	0.05	0.05	0.09	0.03
Lu	0.02	0.02	0.01	0.05	0.02	0.01	0.01	0.01	0.01	0.01	0.00
Hf	0.09	0.17	0.10	0.41	0.12	0.03	0.00	0.00	0.00	0.00	bdl
Ta	0.01	0.01	0.02	0.05	0.01	0.00	0.00	0.00	0.00	0.00	bdl
Pb	0.48	0.57	0.89	3.43	0.48	0.43	0.69	0.91	1.81	0.68	1.09
Th	0.63	1.45	0.33	8.45	0.28	0.24	0.11	0.03	0.00	0.01	0.00
U	0.13	0.27	0.18	1.85	0.13	0.05	0.36	0.13	0.02	0.01	0.12
∑REE	89.5	71.0	71.4	183.0	86.6	78.1	70.3	51.1	60.4	70.4	41.6
LREE/HREE	72.8	59.1	78.0	58.1	74.3	172.1	44.2	64.0	77.4	54.2	68.5
δEu	1.23	1.48	1.63	1.53	1.40	1.48	0.65	0.78	0.83	0.79	1.04
La/Ho	565	568	664	450	635	1791	418	710	915	536	890
Y/Ho	28.5	27.8	27.2	26.7	26.7	31.5	30.8	27.5	29.5	32.1	28.2
Sm/Nd	0.08	0.10	0.10	0.10	0.09	0.06	0.13	0.11	0.10	0.11	0.10

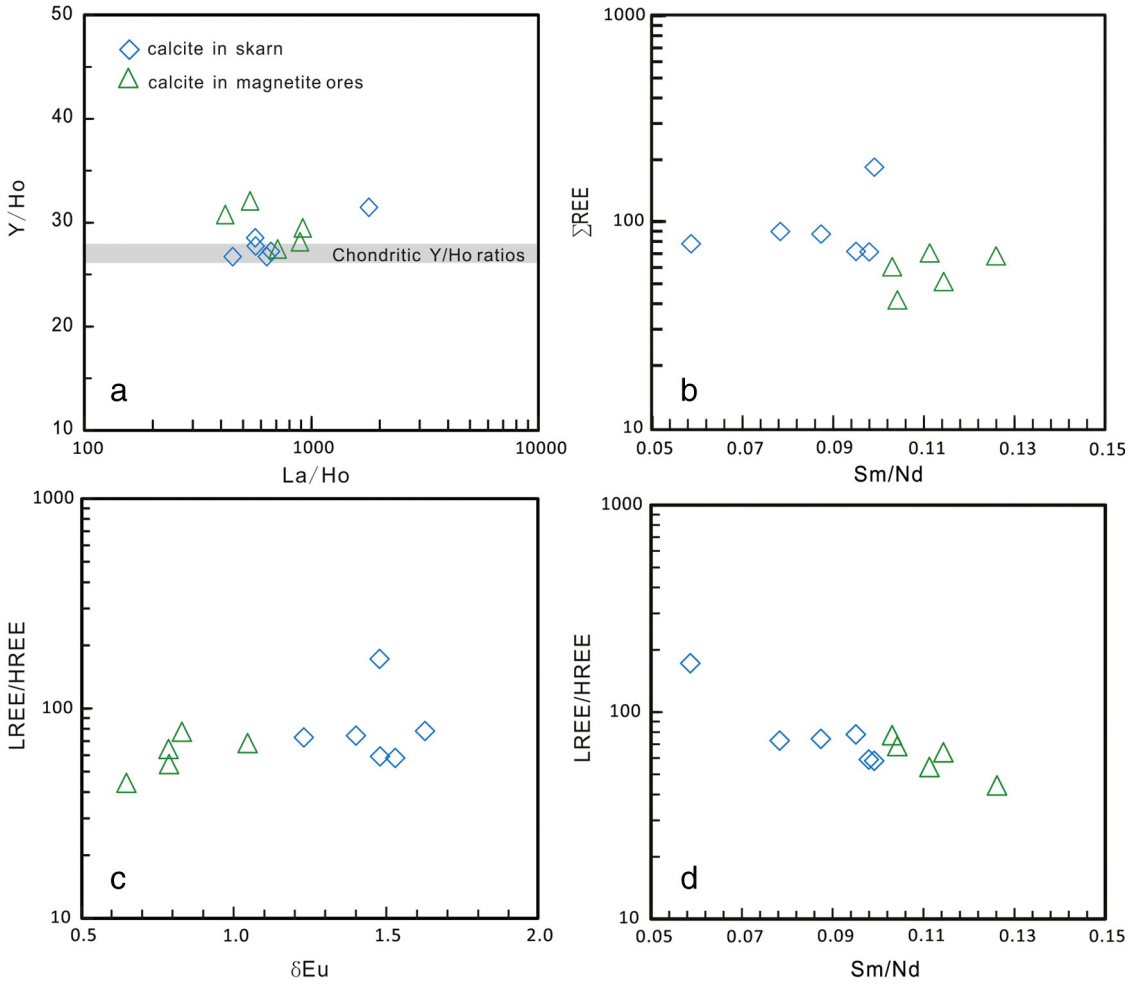

Fig. 4. Covariance plots of calcite: (a) LREE/HREE vs. Sm/Nd; (b) LREE/HREE vs. δEu; (c) ∑REE vs. Sm/Nd; (d) Y/Ho vs. La/Ho.

the upper limit (600 °C) of the Heating–Freezing System. The V-type FIs data were not further discussed because calcite is susceptible to cracking at above 400 °C, making the data reliability questionable. Halite is the only daughter mineral identified in the analyzed S-type FIs. We did not measure the first melting temperatures of the S-type FIs and consider all of them as NaCl-H_2O aqueous system.

The features and microthermometric results of the four FI types are summarized in the Tables 4 and 5. The first melting temperatures of the FIs vary from −73.5 °C to −32.9 °C with two dominant temperature ranges, i.e., −73.5 °C to −70.3 °C and −50.8 °C t − 48.2 °C (Fig. 7). The C1 FIs include L-, S- and PL-type, with their homogenization temperatures being 140 °C to 324 °C and salinities being 0.2 wt.% to 40.1 wt.% NaCl equiv. (Fig. 8a). The C2 FIs include L-, S-, PL- and V-type, with their homogenization temperatures being 106 °C to 364 °C and salinities being 11.7 wt.% to 41.5 wt.% NaCl equiv. (Fig. 8b).

6. Discussion

6.1. Ore-forming processes

Calcite is a common gangue mineral in hydrothermal ore deposits, and it always incorporates trace amounts of REE. The systematics between the REE makes them extremely useful for understanding a variety of chemical processes in the geological environment (Henderson, 1984; Taylor and McLennan, 1988). Many hydrothermal processes would lead to REE fractionation, and thus calcite REE signatures can serve as proxies to backtrack the ore-forming hydrothermal processes (e.g., Bau and Moller, 1992; Sverjensky, 1984; Debruyne et al., 2016).

C1 and C2 possess high LREE/HREE from 44 to 172, implying REE fractionation have occurred and led LREE enrichment over HREE in calcite. REE fractionation is controlled by several processes, including sorption and complexation along the fluid flow pathway, coprecipitation and mineralogical control of calcite at the deposition sites, together with remobilization after its deposition (Bau and Moller, 1992; Debruyne et al., 2016). Sorption is expected to preferentially remove HREE but the rate decreases with increasing temperature (Bau, 1991). At the high-temperature hydrothermal conditions (up to 360 °C at Dunde), complexation may have prevailed over sorption along the flow pathway. Under slightly acidic environment (e.g., with NaCl-rich mineralizing fluids; Muchez and Corbella, 2012), the HREE-selective OH^- and CO_3^{2-} complexes are unlikely to be the main transporting species, and the LREE-selective Cl (±F) complexes may have contributed to the LREE enrichment. The coprecipitating minerals of the calcite, in this case, mainly are garnet, diopside and magnetite. Both the skarn and magnetite ore display LREE-enrich patterns (Fig. 5c), implying the insignificant effect of the coprecipitation on the calcite. Considering the mineralogical control of calcite, the partition ratios decrease systematically from LREE to HREE (Zhong and Mucci, 1995). Thus, calcite has a preference for LREE over HREE during precipitation, resulting in the preferential LREE

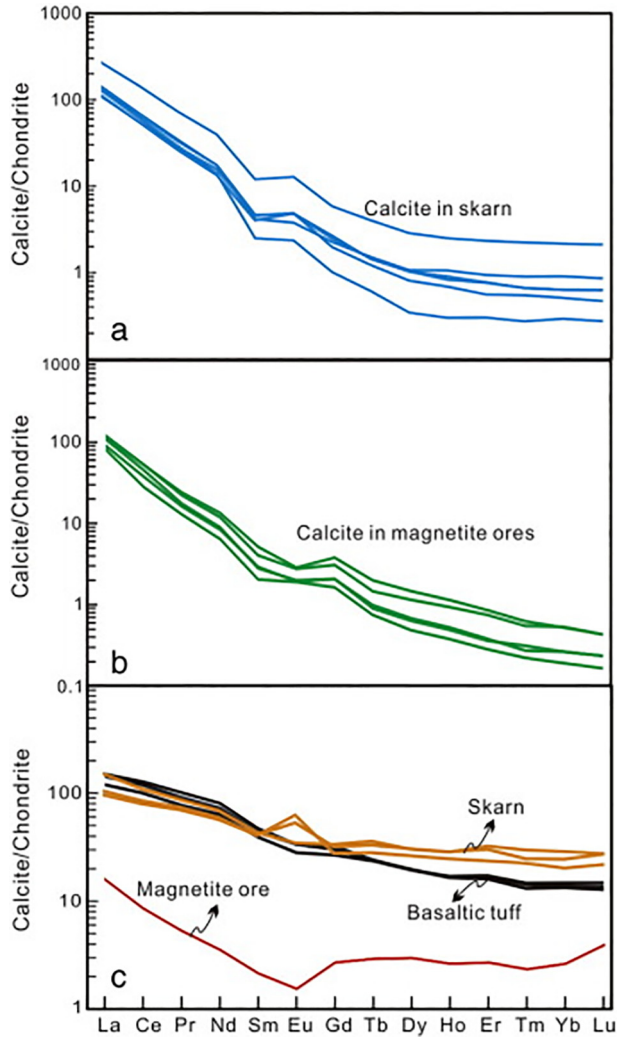

Fig. 5. Chondrite-normalized REE patterns for (a) calcite in the skarn, (b) calcite in the magnetite ores and (c) basaltic tuff, skarn and magnetite ore (data from Duan et al., 2014 and Ge, 2013) from the Dunde iron–zinc deposit. Normalization values from Sun and McDonough (1989).

Table 2
Carbon and Oxygen isotopic compositions of the calcite from the Dunde iron–zinc deposit. $\delta^{18}O_{V\text{-}SMOW\text{-}fluid}$ (‰) = $\delta^{18}O_{V\text{-}SMOW\text{-}calcite}$ (‰) − $1000\ln\alpha_{calcite\text{-}water}$, $1000\ln\alpha_{calcite\text{-}water} = 4.01 \times 10^6/T^2 - 4.66 \times 10^3/T + 1.71$, scope of temperature (T/°C): 0–1200 °C, suggested by Zheng (1999).

Sample	$\delta^{13}C_{V\text{-}PDB}$ (‰)	$\delta^{18}O_{V\text{-}SMOW}$ (‰)	Average T_m (°C)	$\delta^{18}O_{V\text{-}SMOW}$(‰)$_{fluid}$
13DD-3	0.16	11.47	190	1.47
Repeated	0.05	11.36	190	1.36
13DD-4	0.31	10.65	190	0.65
13DD-6	0.08	10.03	190	0.03
Repeated	0.06	10.18	190	0.18
13DD-7	0.47	10.07	190	0.07
Repeated	0.25	9.22	190	−0.78
13DD-8	0.38	10.37	190	0.37
Repeated	0.39	10.7	190	0.7
13DD-9	0.19	11.54	190	1.54
Repeated	0.26	11.85	190	1.85
13DD-21	0.74	14.39	249	2.99
13DD-22	0.75	14.57	249	3.17
13DD-23	0.37	14.96	249	3.56
13DD-24	0.67	14.15	249	2.75
13DD-32	0.21	15.22	249	3.82
11DD-1	0.77	13.55	249	2.15
11DD-2	0.85	13.82	249	2.42
11DD-3	0.66	13.8	249	2.4
11DD-4	0.76	13.96	249	2.56
11DD-5	0.39	13.96	249	5.46
11DD-6	0.86	13.66	249	2.26
11DD-7	0.72	14.63	249	3.23

Table 3
Sr isotopic compositions of the calcite from the Dunde iron–zinc deposit.

Sample	Rb (ppm)	Sr (ppm)	Rb/Sr	$^{87}Sr/^{86}Sr$	2δ
13DD-3	0.42	201	0.0021	0.707230	0.000014
13DD-4	0.16	182	0.0009	0.707790	0.000014
13DD-6	0.39	170	0.0023	0.707476	0.000017
13DD-7	0.25	164	0.0015	0.707636	0.000016
13DD-8	0.12	197	0.0006	0.707234	0.000016
13DD-9	0.10	191	0.0005	0.707198	0.000011
13DD-21	0.05	255	0.0002	0.707160	0.000007
13DD-22	0.07	181	0.0004	0.707246	0.000007
13DD-23	0.06	238	0.0003	0.707148	0.000007
13DD-24	0.05	268	0.0002	0.707208	0.000008
13DD-32	0.10	270	0.0004	0.707345	0.000008

enrichment in calcite. No growth zonation or recrystallization was observed in the Dunde calcite, suggesting that post-depositional remobilization was also unlikely. To summarize, the Cl (±F) complexation along the fluid flow pathway and mineralogical control of calcite at the deposition sites were responsible for the LREE enrichment in calcite.

Yttrium and Ho are regarded as geochemical twins and behave coherently in most geological environments, leading to the maintenance of the chondritic Y/Ho ratio (ca. 26–28) in common igneous rocks and epiclastic sediments (Bau and Dulski, 1999; Webb and Kamber, 2000). The analyzed C1 and C2 contain Y/Ho of 26.7 to 32.1, most of which are chondritic and similar to the unaltered volcanic host rocks (ca. 27–30, Table S1). The superchondritic Y/Ho may be attributed to the Y–Ho fractionation during the calcite precipitation as calcite has a mineralogical preference for Ho (Tanaka and Kawabe, 2006; Tanaka et al., 2008). Bau and Dulski (1995) proposed that Y/Ho variation in co-genetic hydrothermal minerals is negligible, compared to La/Ho variation by studies of the fluorite and calcite. The narrow Y/Ho range of the analyzed calcite showed the same distribution characteristic in the Y/Ho-La/Ho diagram (Fig. 4a), indicating that all the analyzed calcite is likely co-genetic. This is further evidenced by the linear correlation shown in the LREE/HREE versus Sm/Nd, ∑REE versus Sm/Nd and LREE/HREE versus δEu diagrams (Fig. 4b–d).

As for the Eu anomaly of calcite, C1 has positive Eu anomaly (δEu: 1.23–1.63) while C2 has negative Eu anomaly (δEu: 0.65–0.83) except for one with slightly positive Eu anomaly (δEu = 1.04) (Fig. 5a, b). Thermodynamic calculations and theoretical considerations suggest that temperature is the most important parameter in controlling the Eu^{3+}/Eu^{2+} redox potential in hydrothermal systems: When temperatures exceeds 250 °C, Eu^{2+} dominates over Eu^{3+} in fluids, leading to positive Eu anomaly in the precipitated mineral (Sverjensky, 1984; Bau and Moller, 1992). Microthermometric results of FIs suggest that the average temperature of the fluid in C1 is 190 °C. At temperatures below 200 °C, Eu is mostly trivalent and is less fractionated from its neighboring REE. The Dunde skarn contains positive Eu anomaly (1.46–2.55) (Fig. 5c), thus the observed positive anomaly in C1 may have been inherited from its parental skarn alteration fluids. In contrast, the average temperature of the fluids in C2 is 249 °C. At this temperature, Eu^{2+} is expected to dominate the parental fluids and C2 should have displayed positive Eu anomaly. The ionic radius of Sr^{2+} (118 pm) is similar to that of Eu^{2+} (117 pm), and thus Sr^{2+} is a good geochemical analog for Eu^{2+} in the calcite mineral lattice (Shannon, 1976). Strontium concentration (181–270 ppm,

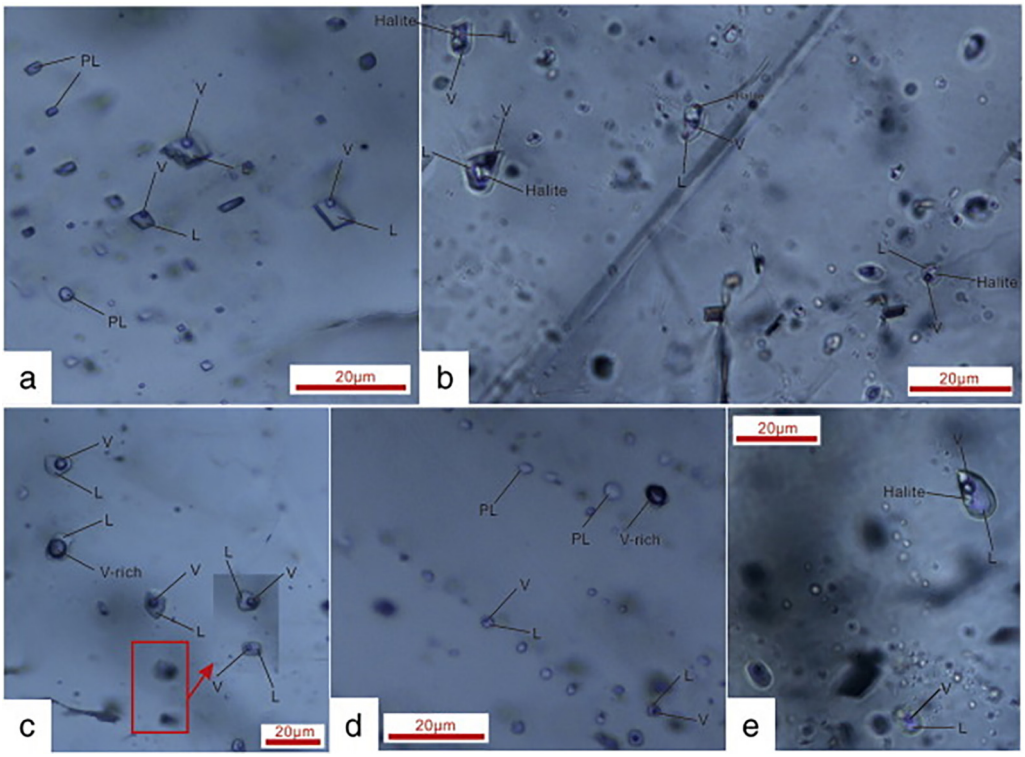

Fig. 6. Photomicrographs of the fluid inclusions in the Dunde iron–zinc deposit. (a) coexistence of liquid-rich FIs and pure liquid FIs, (b) halite-bearing FIs in C1 calcite; (c) coexistence of liquid-rich FIs and vapor-rich FIs, (d) coexistence of liquid-rich FIs, vapor-rich FIs and pure liquid FIs, (e) halite-bearing FIs in C2 calcite. Abbreviation: L: liquid phase, V: vapor phase, PL: pure liquid, V-rich: vapor rich.

Table 4
Overview of fluid inclusion types in calcite from the Dunde iron–zinc deposit.

Type	Fluid phases	Daughter minerals	Size (μm)	Vol.%	Shape	Occurrence	Location
L	V_{H2O} + L_{H2O}		3–30	5–60	Oval, rectangular or irregular	Random distributions or in clusters	C1,C2
S	V_{H2O} + L_{H2O}	Halite	4–21	5–40	Oval, rectangular or irregular	Random distributions or in clusters	C1,C2
V	V_{H2O} + L_{H2O} or V_{H2O}			>80	Oval, triangle, rectangular or irregular	Isolated, random distributions or in clusters	C2
PL	L_{H2O}		2–15		Oval, triangle, rectangular	In clusters	C1,C2

Abbreviations: V_{H2O} = H_2O vapor; L_{H2O} = H_2O liquid; vol.% = volume percentage of the vapor phase; C1: calcite in skarn,C2: calcite in magnetite.

Table 5
Microthermometric data of fluid inclusions in calcite from the Dunde iron deposit.

Occurrence	Type	Number	Ti (°C)	Tm,ice (°C)	Tv (°C)	Tm,hal (°C)	Th (°C)	Homogenization state	Salinity (wt.% NaCl)
Calcite in skarns	L-type	40	−50.1 to −49.2	−26 to −0.1			140 to 274	Liquid	0.2 to 26.2
	S-type	9			110 to 221	171 to 324	171 to 324	Liquid	30.5 to 40.1
Calcite in magnetite	L-type	48	−73.4 to −32.9	−34.1 to −8.0			106 to 364	Liquid	11.7 to 31.4
	S-type	13			91 to 354	161 to 334	224 to 354	Liquid	30.1 to 41.5

Abbreviations: Ti (°C) = first ice-melting temperature; Tm,ice (°C): temperature of ice point; Tv (°C) = bubble disappearance temperature; Tm,hal (°C) = melting temperature of halite; Th (°C) = final homogenization temperature.

242 ppm on average) of C2 is much higher than that of C1 (164–201 ppm, 181 ppm on average), so the partition ratio of Eu^{2+} is likely to be much lower than the highly compatible trivalent REE in C2. As a result, C2 shows slightly positive or even negative Eu anomaly.

6.2. Ore-forming fluids components

Studies of FIs in calcite could constrain the hydrothermal evolution of the mineralization. Microthermometric analyses yielded a wide range of homogenization temperatures (106 °C to 364 °C) with variable salinities (0.2 wt.% to 41.5 wt.% NaCl equiv.). Thus, the components of the ore-forming fluid are expected to be complex. Meanwhile, the first melting temperatures of the FIs are also highly variable (−73.5 °C to −32.9 °C) (Fig. 7). Two intervals, namely, −73.5 °C–−70.3 °C and −50.8 °C–−48.2 °C, dominant the temperature range, suggesting that the ore-forming fluids predominantly consisted of brine-featured fluid and $CaCl_2$-H_2O aqueous fluid, with possibly, minor $MgCl_2$-H_2O and $FeCl_2$-H_2O aqueous fluids. The presence of abundant halite-bearing FIs implies that the NaCl-H_2O aqueous system was also a major component of the ore-forming fluids. The fluid salinity–temperature diagram (Fig. 8a, b) suggests three distinct fluid types, i.e., high-, medium- and low-salinity fluids, were involved in the ore-forming processes. The

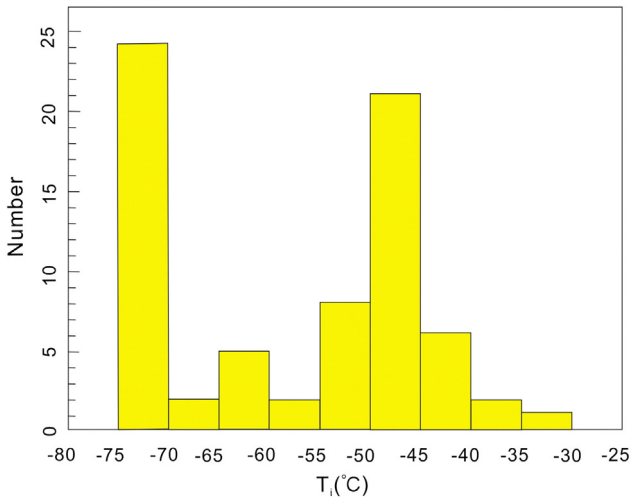

Fig. 7. Histogram of the first ice melting temperatures of the fluid inclusions in the calcite from the Dunde iron–zinc deposit.

high-salinity (>35 wt.% NaCl equiv.) and medium-to-high temperatures (205 °C–354 °C) aqueous fluids, mainly occur in the halite-bearing FIs from both C1 and C2. The medium-salinity (10–35 wt.% NaCl equiv.) aqueous fluids (with a wide temperature range: 106 °C–364 °C) were characterized by the $CaCl_2$-H_2O and brine-featured aqueous system, and occur also in both C1 and C2. The low-salinity (<10 wt.% NaCl equiv.) and low-to-medium temperature (106 °C–223 °C) aqueous fluids may represent seawater/meteoric water, which occur only in C1. The spatial coexistence of the above FI types within the same assemblage (Fig. 6) also suggest that both fluids may have been present during the calcite precipitation within the timeframe of the iron mineralizing episode.

For many hydrothermal deposit types, high-salinity fluids play an important role in metal transport (e.g., Webster, 1997; Richards, 2015). The solubility of iron depends on the activity of Cl^- and the moderate- to high-salinity fluids favor Fe transportation in the form of chloride complexing (Bell et al., 2011). Chlorite alteration is widespread at Dunde, with abundant Cl-rich minerals (e.g., ferropargasite and apatite) (Fig. 3e, f) occurring in the pre- and syn-mineralization stages (Duan et al., 2014; Ge et al., 2014). However, the source of the high-salinity fluid has long been in debate, i.e., magmatic versus non-magmatic source (e.g., Xavier et al., 2008; Torresi et al., 2012; Lecumberri-Sanchez et al., 2015). The calculated $\delta^{18}O$ compositions (−0.78‰–5.46‰) of the fluid in equilibrium with calcite suggest that a magma source was responsible for the ore-forming fluids. Moreover, the $\delta^{34}S$ (3.8‰–8.1‰, averaging 6.8‰) of the fluid in equilibrium with sulfides (pyrrhotite, sphalerite, pyrite, and loellingite) was thought to be generated from a magma source under high-fO_2 condition (Duan et al., 2014). Therefore, we propose that the Dunde high-salinity fluids were likely magma-derived.

Given that the Dunde deposit formed in a submarine environment, the low-salinity fluids were most likely from the seawater instead of meteoric water. Radial faults are widespread at Dunde, which may have allowed seawater to circulate through the magmatic-hydrothermal system, as supported by the elevated temperature of these low-salinity fluids. The consequent fluid–rock interactions may have generated the resultant medium-salinity $CaCl_2$-H_2O aqueous and brine-featured fluids, which became an important component of the ore-forming fluids.

6.3. Fluid sources

Hydrothermal calcite precipitation is generally controlled by three processes: fluid mixing, CO_2 degassing and fluid–rock interactions (Zheng, 1990; Zheng and Hoefs, 1993). Carbon- and oxygen isotopes of calcite could provide constraints on the calcite precipitation mechanism. C1 and C2 are relatively homogeneous in carbon- and oxygen isotopes, implying fluid mixing should not be the dominant factor (e.g., Peng and Hu, 2001; Wang et al., 2012), which is also evidenced by the narrow Y/Ho range. In addition, no evidence of CO_2 degassing was found through fluid inclusion studies, even though the absence of fluid boiling could not preclude a slow CO_2 degassing (Zheng, 1990). Thus, CO_2 degassing is also ruled out as a possible mechanism causing calcite precipitation. In Fig. 9, $\delta^{13}C$ for both C1 and C2 is comparable with the marine carbonates, whereas their $\delta^{18}O$ is consistently lower than the latter ($\delta^{13}C = 0‰ \pm 4‰$, $\delta^{18}O = 20‰–24‰$, Veizer and Hoefs (1976) and Hoefs (1997)). The samples fall in the field of the dissolution of the marine carbonate, suggesting the formation of calcite results from the fluid–limestone interaction. Moreover, the Dunde calcite $\delta^{13}C$ and $\delta^{18}O$ are similar to the Bugula carbonates (Fig. 9). Yang et al. (2014) proposed that the Bugula carbonates were derived from carbon released by the subducted oceanic sediments and recycled by alkaline arc-related magma. Given that the Dunde deposit is hosted in the intensively altered andesitic-basaltic rocks (Fig. 2a), we proposed that the volcanic wall rocks may also

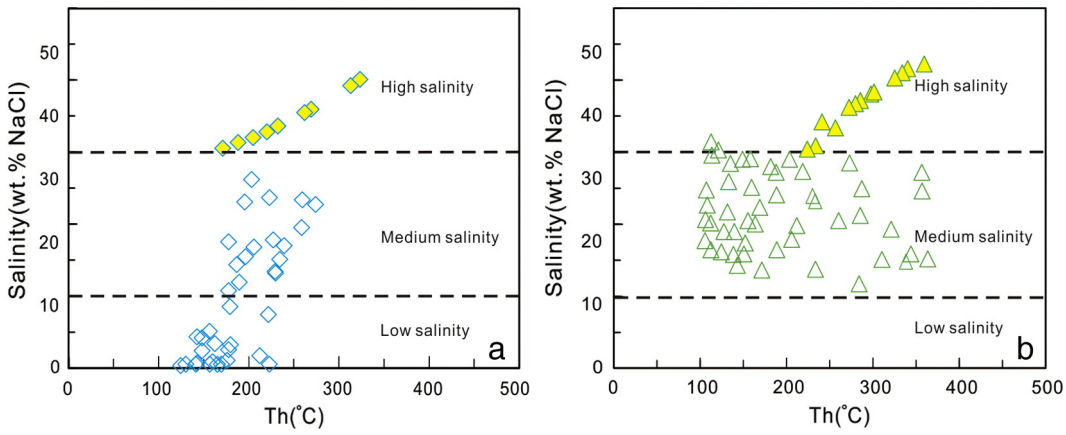

Fig. 8. Salinities versus homogenization temperatures of fluid inclusions in the calcite from the Dunde iron–zinc deposit (blue diamond for C1 data, green triangle for C2 data; open symbol for liquid-rich FI data, close symbols for halite-bearing FI data). (For interpretation of the references to color in this figure legend, the reader is referred to the web version of this article.)

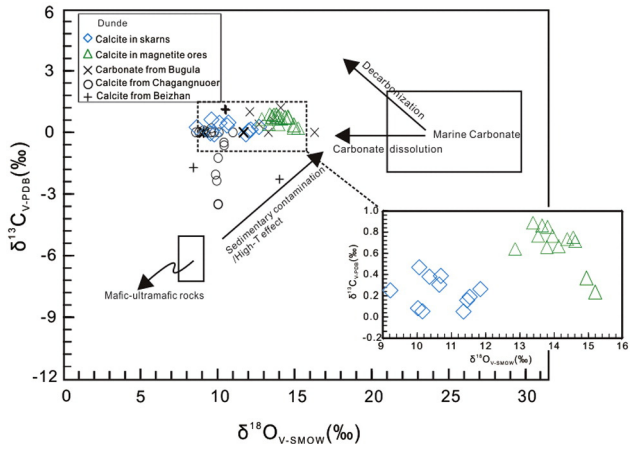

Fig. 9. Carbon and oxygen isotopic compositions of calcite/carbonate from Dunde, Chagangnuoer, Beizhan and Bugula (Yang et al., 2014) in the Awulale Mountains. Carbon and oxygen isotopes of marine carbonate (Hoefs, 1997) and mafic-ultramafic rocks (Bell and Simonetti, 2010) are shown for comparison.

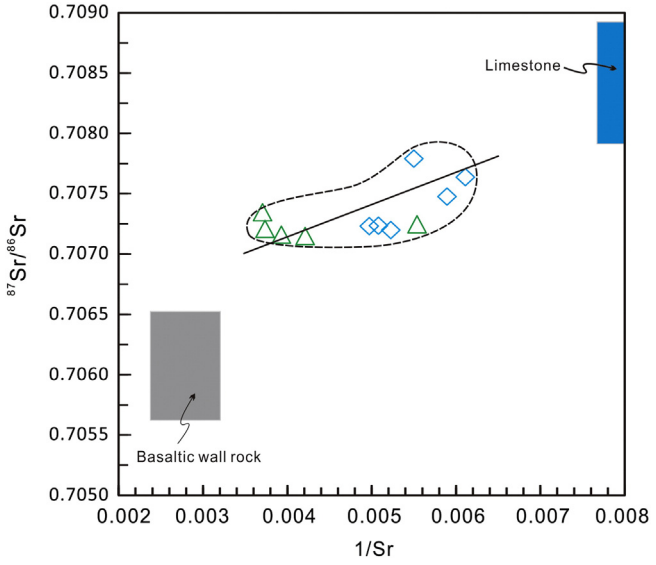

Fig. 10. $^{87}Sr/^{86}Sr$ versus 1/Sr for the calcite in the Dunde iron–zinc deposit, compared with the Sr isotopic composition of the wall rocks and Late Carboniferous limestone. The data for the basaltic wall rocks are from Li et al. (2015b), Yan et al. (2015) and Yang et al. (2012), and the data of limestone/seawater are from Bruckschen et al. (1999) and Veizer (1989). Symbology as in Fig. 4.

contribute to the $\delta^{13}C$ and $\delta^{18}O$ compositions of the calcite via fluid–rock interactions.

Hydrothermal calcite inherits $\delta^{13}C$ almost directly from parental fluids because of the insignificant fractionation as a function of temperature, and its $\delta^{18}O$ is a function of the parental fluid's $\delta^{18}O$ plus the isotopic fractionation between calcite and the fluids (e.g., Ohmoto, 1972; Zheng, 1999). Thus, it is reasonable to assume that the calcite $\delta^{13}C$ approximate the parental fluid, whereas the calcite $\delta^{18}O$ represent the parental fluid's $\delta^{18}O$ but with isotopic fractionation. The $\delta^{18}O$ of water in equilibrium with calcite was calculated based on the average of FI homogenization temperatures and calcite-water oxygen isotopic equilibrium fractionation factor suggested by Zheng (1999). Given the oxygen of the parental fluids is almost totally in water, the calculated $\delta^{18}O_{H2O}$ should approximate the parental fluid's $\delta^{18}O$. The calculated $\delta^{18}O_{H2O}$ is of −0.78‰–1.85‰ for C1 and 2.15‰–5.46‰ for C2 (Table 2). The results overlap the lowest limit for the magmatic water ($\delta^{18}O$ = 5.5‰–9.0‰; Ohmoto (1972) and Sheppard (1986)), but the more ^{18}O-delepted values point to the seawater involvement. The $\delta^{18}O$ difference between the fluids in equilibrium with C1 and C2 may be attributed to the different degree of mixing between magmatic fluids and seawater, and more seawater may have been involved in the C1 parental fluids.

6.4. Fluid passages

Calcite C- and O isotopes are useful in tracking the fluid sources, while calcite Sr isotope can determine the fluid passages (e.g., Wen et al., 2014; Deng et al., 2015; Pokrovsky and Bujakaite, 2015). In the lattice of calcite ($CaCO_3$), Ca^{2+} (0.1 nm) can be substituted by the similar size Sr^{2+} (0.118 nm) but not the bigger Rb^{+} (0.152 nm), resulting in extremely low Rb/Sr. Thus, the radiogenic ^{87}Sr accumulation by ^{87}Rb decay is very limited in the present-day calcite Sr isotopic composition. The measured calcite $^{87}Sr/^{86}Sr$ isotope represents approximately the Sr isotopic composition of its parental fluids when calcite was precipitated (e.g., Hecht et al., 1999; Peng and Hu, 2001).

As the Dunde iron–zinc deposit is hosted in the Late Carboniferous Dahalajunshan Formation volcanic-volcanoclastic rocks, the ore-forming fluids inevitably inherited the Sr isotope composition of these volcanic wall rocks as the fluids circulated through the volcanic rocks. In fact, initial $^{87}Sr/^{86}Sr$ of the Late Carboniferous Dahalajunshan Formation volcanic rocks exhibits a narrow compositional range of 0.7032 to 0.7058 (e.g., Zhu et al., 2006, 2009; Li et al., 2015b). However, at the time when Dunde deposit formed, the Dunde volcanic rocks would have acquired higher whole-rock $^{87}Sr/^{86}Sr$ due to ^{87}Rb decay. A latest mineralization age of 300 Ma was used to recalculate the $^{87}Sr/^{86}Sr$ values of the wall rocks. The $^{87}Sr/^{86}Sr$ is estimated to range from 0.7056 to 0.7066, which is still lower than the calcite $^{87}Sr/^{86}Sr$ values (0.7071–0.7078). Thus, a higher $^{87}Sr/^{86}Sr$ reservoir may have contributed to the ore-forming fluids. For the Dunde case, seawater and limestone wall rocks may play the role. Seawater Sr isotopic composition in certain geological time is quite homogeneous, and Sr isotopes do not fractionate during the course of carbonate precipitation from seawater (Veizer, 1989), so the $^{87}Sr/^{86}Sr$ ratios of contemporary marine carbonates are uniform worldwide. The Sinian global seawater $^{87}Sr/^{86}Sr$ is around 0.709 (or slightly lower), while post-Sinian one is <0.709 (Burke et al., 1982; Veizer, 1989; Veizer et al., 1997, 1999). Carbonate rocks of Mesoproterozoic, Silurian, Devonian and Carboniferous ages are abundant in the AMB, with nearly a 300-m-thick limestone in the Dahalajunshan Formation alone (Zhang et al., 2012a). As shown in the Fig. 2b, limestone is intercalated with the volcanic wall rocks at Dunde. The Silurian, Devonian and Late Carboniferous seawater have $^{87}Sr/^{86}Sr$ isotopic compositions from 0.7075 to 0.7089 (Veizer, 1989; Bruckschen et al., 1999), higher than most of Dunde calcite. Thus, the seawater/limestone could act as the reservoir with higher Sr isotopic compositions. In Fig. 10, the positive correlation between $^{87}Sr/^{86}Sr$ and 1/Sr reflects mixing of two distinct sources, namely the basaltic/andesitic volcanic wall rocks (with high Sr content and low $^{87}Sr/^{86}Sr$) and the limestones/seawater (with low Sr content and high $^{87}Sr/^{86}Sr$).

6.5. Implications for the iron mineralization

The Dunde iron–zinc deposit is typical of the SVIO deposit in the ABM. Genesis of the Dunde deposit, may have been similar to other Tianshan SVIO deposits, such as Chagangnuoer, Zhibo, Beizhan and Shikebutai in the western Tianshan and Yamansu in the eastern Tianshan. A magmatic origin was suggested for the Chagangnuoer and Zhibo deposits, as they contain abundant magmatic-type massive or crypto-explosive brecciated magnetite ores (Feng et al.,

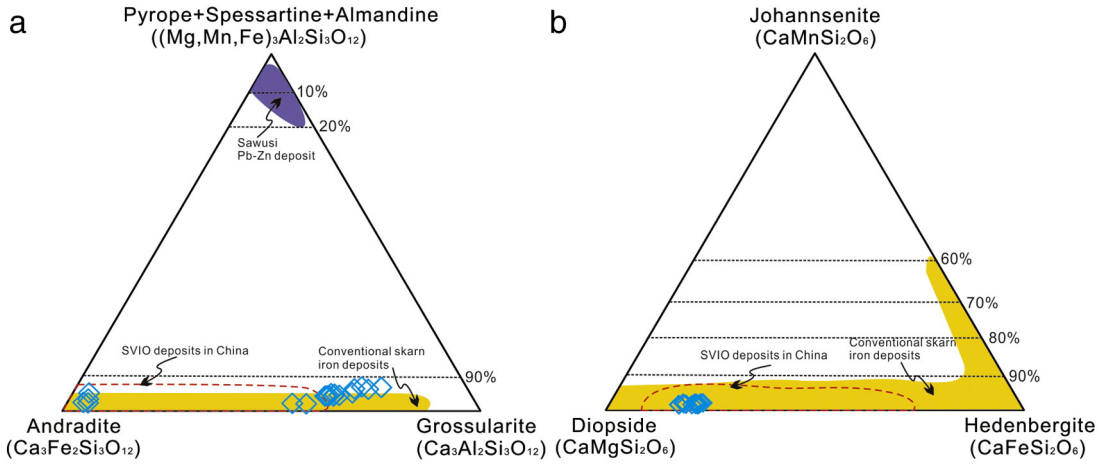

Fig. 11. Ternary plots for (a) garnet and (b) clinopyroxene composition for the Dunde deposit. The Sawusi data are from Liu et al. (2012), the Chinese iron deposits (related to submarine volcanic rocks) data are from Xu et al. (2010) and Hong et al. (2012), and the typical iron skarn data are from Meinert et al. (2005).

2010; Wang et al., 2011; Zhang et al., 2014). However, these ores contain very low P and Ti contents and have no correlation among P, Ti and FeO^T, which are inconsistent with the oxide melt immiscibility/fractional crystallization from the silicate magma. At Dunde, the massive magmatic ores more or less exhibit hydrothermal alteration features, such as the presence of interstitial skarn minerals. This suggests that a silicate liquid immiscibility genesis is unlikely for the Dunde deposit. The lack of chemical exhalites, e.g., pyritic chert, jasper and Fe-Mn oxide in the Dunde deposit, contradicts the hypothesis of exhalative syn-sedimentary genesis. Typical volcanic exhalative syn-sedimentation deposits are characterized by Mn- and Mg-rich skarn minerals such as spessartine and almandine (e.g., Liu et al., 2012), whereas the Dunde skarn minerals are mostly Ca-rich including grossularite, andradite and diopside, resembling many SVIO deposits and typical skarn iron deposits (Fig. 11). By elimination, we endorse that the Dunde deposit is of skarn genesis, also because: (1) skarn is widely developed around wall rocks and orebodies; (2) the mineral assemblage of garnet, diopside and epidote is typical of skarn iron deposits; (3) paragenetic texture between the skarn minerals and magnetite are well displayed under the microscope.

Many models were proposed for the skarn formation, including metasomatism along shear zones, intrusion-related and volcanic-related. The skarn-associated fractures at Dunde are short but wide, showing various orientations and are mainly volcano-related radial fractures (Feng et al., 2010). Skarn alteration at Dunde is closely associated with the basaltic and andesitic volcanic rocks, both of which are Ca-rich. The skarn comprises predominantly Ca-rich minerals including grossularite, andradite and diopside (Fig. 11). The Dunde skarn also contains similar REE contents and patterns to the basaltic tuff (Fig. 5c), and can thus be the alteration products of the latter. This is also supported by the direct contact relationship between basaltic tuff and skarn at the Dunde ore district. To determine the gains and losses of basaltic tuff during the hydrothermal alteration, mass balance calculation was performed with the major elements of the basaltic tuff and skarn based on the isocon method suggested by Grant (1986). A fresh basaltic tuff sample (Sample DD007, LOI = 0.37 wt.%) and a massive garnet skarn sample (Sample DD006) (Table 6), collected near each other, were used for the calculation. $\Delta C_i/C_i^O$ was used as a proxy to indicate the gain (positive values) and loss (negative values) relative to the original rock. Constant alumina and constant volume were assumed for mass balance calculation, respectively and yielded similar results (Table 6). The results suggest an overall rock mass gain of 20% and 21% while holding alumina and volume constant, respectively. The major changes include gaining of 39% Ca, 59% Fe and 55% Mg and loss of 55% K, 33% Na and 44% Ti in comparison with the basaltic tuff (Table 6, Fig. 12a). The Ca gain was

Table 6
Geochemical compositions of basaltic tuff and skarn according to Ge (2013) and related mass-balance calculations based on constant aluminum and constant volume according to Grant (1986).

Sample	Original rock Basaltic tuff (DD007)	Altered rock Skarn (DD006)	Constant aluminum $\Delta C_i/C_i^O$	Constant volume $\Delta C_i/C_i^O$
SiO_2	47.47	44.92	0.14	0.13
TiO_2	2.00	0.93	−0.44	−0.45
Al_2O_3	11.81	9.84	0.00	−0.01
$Fe_2O_3^T$	7.64	10.13	0.59	0.58
MnO	0.99	0.91	0.11	0.10
MgO	3.98	5.13	0.55	0.54
CaO	22.75	26.25	0.39	0.38
Na_2O	0.91	0.51	−0.33	−0.34
K_2O	1.77	0.71	−0.52	−0.52
P_2O_5	0.33	0.32	0.17	0.17
LOI	0.37	0.94	2.05	2.03
Sum	100.02	100.59	0.21	0.20
ρ (g/cm^3)	2.82	3.36		

Notes: calculation formula with assumed constant aluminum: $C_i^A = (C_{Al2O3}^A/C_{Al2O3}^O) \times (C_i^O + \Delta C_i)$; calculation formula with assumed constant volume: $C_i^A = (\rho^O/\rho^A) \times (C_i^O + \Delta C_i)$. $\Delta C_i/C_i^O$: the change in concentration of oxide i relative to that of the original rocks; positive value means gain, whereas negative value means loss. LOI = loss on ignition; ρ = density.

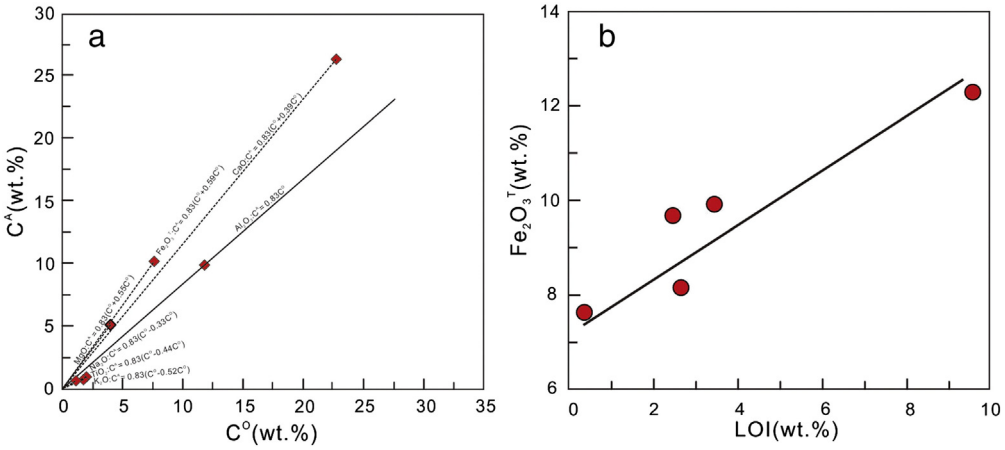

Fig. 12. (a) Isocon diagrams after the mass-balance calculation between fresh basaltic tuff (DD007) and skarn (DD006). The isocon line for Al_2O_3 corresponds to $\Delta C_i^O / C_i^O = 0$ and is designated $C^A = 0.83C^O$. All components for which the gains or losses relative to C_i^O are plotted on a line radiating from the origin; (b) $Fe_2O_3^T$ versus LOI.

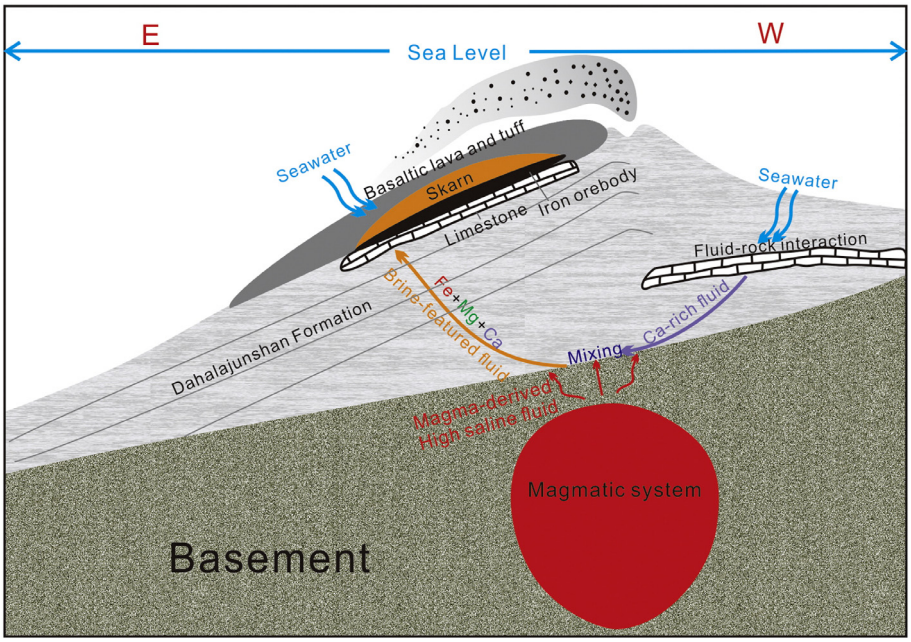

Fig. 13. Schematic diagram for the Dunde iron mineralization model. modified after Hou et al. (2014b)

most likely from the limestone dissolution. The positive correlation between $Fe_2O_3^T$ and the loss-on-ignitions (LOIs) (Fig. 12b) of the basaltic wall rocks also implies the introduction of iron by the hydrothermal fluids. The introduction of Fe and Mg may point to a deep-seated magmatic system. Duan et al. (2014) proposed a buried dioritic intrusion may have been responsible for the deep-seated magmatic system, whereas Hou et al. (2014b) and Li et al. (2014) suggest it is a shallow magma chamber that plays the role. Characterization of this deep-seated magmatic system is still inadequate and requires further investigation.

Based on the above discussion, we envisage a new genetic model for the Dunde deposit. We propose that both the basaltic wall rocks and the limestone may have participated in the ore-forming processes, yet the majority of the iron was likely to be introduced by a deep-seated magmatic system, whose exact nature is yet to be fully understood. As shown in the Fig. 13, the seawater may have percolated down the fractures and be heated by the magmatic system, accompanied by the exsolved fluid to generate a chloride-bearing fluid circulation. This is supported by the high chlorine solubility in the basaltic melt (up to 2.9 wt.% at 200 MPa; Webster et al., 1999). As for the Dunde case, at the physicochemical conditions (T: >986 °C, P: 120–200 MPa, logfO_2: FMQ − 0.4; Li et al., 2015b), chlorine partition coefficients between Cl-bearing fluid and basaltic melt approximate between 2 and 9 (e.g., Alletti et al., 2009; Baker and Alletti, 2012; Beermann et al., 2015). Meanwhile, the magmatic system may have released Fe-Mg-bearing fluids during the exsolution, which ascended to react with the limestone and became Ca-, Fe- and Mg-rich. The fluids may have also altered the basaltic volcanic rocks to form the widespread Ca-rich skarn, and precipitated magnetite along the fractures. The unloading of Fe and Mg and replenishment of Ca may have made the fluids $CaCl_2$-enriched, and led to the calcite precipitation.

7. Conclusions

(1) The restricted Y/Ho suggests that calcite in the skarn (C1) and magnetite ores (C2) are co-genetic. The Cl (±F) complexation along the fluid flow pathway and mineralogical control of calcite at the depositional sites may have accounted for

the calcite LREE enrichment. The positive Eu anomaly of C1 may have been inherited from the parental skarn alteration fluids, whereas the negative or slightly positive Eu anomaly of C2 may have been resulted from the high Sr^{2+} that suppressed the Eu^{2+} in calcite.

(2) Three kinds of ore-forming fluids, namely high-, medium- and low-salinity fluids, were distinguished. Magmatic fluids and seawater may have generated the high- and low-salinity fluids, respectively, while the medium-salinity fluids were likely to be the products of the fluid–rock interactions.

(3) The basaltic volcanic rocks and limestones may have participated in the Dunde iron–zinc mineralization. The limestone dissolution during the fluid–rock interactions may have provided the Ca needed for the ore-forming fluids, while the Fe and Mg may have been introduced from the deep-seated magmatic system.

Acknowledgments

This work was funded by the National Natural Science Foundation of China (Nos. U1203291, 41373031, 41173040 and 41273056). We thank Neng-Ping Sheng, Xiang-Lin Tu, Xin Li, Cong-Ying Li and Xi-Rong Liang for their laboratory assistance and Prof. Zhen-Hua Zhao for the fruitful discussions. Specially, we thank Prof. Bo Wan and two anonymous reviewers for their constructive suggestions and critical comments, which greatly improve this paper. The GIGCAS contribution number is No. IS-2261.

Appendix A. Supplementary data

Supplementary data to this article can be found online at http://dx.doi.org/10.1016/j.oregeorev.2016.06.024.

References

Allen, M.B., Windley, B.F., Zhang, C., 1993. Paleozoic collisional tectonics and magmatism of the Chinese Tien Shan, Central Asia. Tectonophysics 220, 89–115.

Alletti, M., Baker, D.R., Scaillet, B., Aiuppa, A., Moretti, R., Ottolini, L., 2009. Chlorine partitioning between a basaltic melt and H_2O-CO_2 fluids at Mount Etna. Chem. Geol. 263, 37–50.

Baker, D.R., Alletti, M., 2012. Fluid saturation and volatile partitioning between melts and hydrous fluids in crustal magmatic systems: the contribution of experimental measurements and solubility models. Earth Sci. Rev. 114, 298–324.

Bau, M., 1991. Rare-earth element mobility during hydrothermal and metamorphic fluid-rock interaction and the significance of the oxidation state of europium. Chem. Geol. 93, 219–230.

Bau, M., Dulski, P., 1995. Comparative-study of yttrium and rare-earth element behaviors in fluorine-rich hydrothermal fluids. Contrib. Mineral. Petrol. 119, 213–223.

Bau, M., Dulski, P., 1999. Comparing yttrium and rare earths in hydrothermal fluids from the mid-Atlantic ridge: implications for Y and REE behaviour during near-vent mixing and for the Y/Ho ratio of Proterozoic seawater. Chem. Geol. 155, 77–90.

Bau, M., Moller, P., 1992. Rare-earth element fractionation in metamorphogenic hydrothermal calcite, magnesite and siderite. Mineral. Petrol. 45, 231–246.

Bazhenov, M.L., Collins, A.Q., Degtyarev, K.E., Levashova, N.M., Mikolaichuk, A.V., Pavlov, V.E., Van der Voo, R., 2003. Paleozoic northward drift of the north Tien Shan (Central Asia) as revealed by Ordovician and Carboniferous paleomagnetism. Tectonophysics 366, 113–141.

Beermann, O., Botcharnikov, R.E., Nowak, M., 2015. Partitioning of sulfur and chlorine between aqueous fluid and basaltic melt at 1050 °C, 100 and 200 MPa. Chem. Geol. 418, 132–157.

Bell, A.S., Simon, A., Guillong, M., 2011. Gold solubility in oxidized and reduced, water-saturated mafic melt. Geochim. Cosmochim. Acta 75, 1718–1732.

Bell, K., Simonetti, A., 2010. Source of parental melts to carbonatites-critical isotopic constraints. Mineral. Petrol. 98, 77–89.

Bodnar, R.J., 1994. Synthetic fluid inclusions. 12. The system H_2O-Nacl-experimental-determination of the halite liquidus and isochores for a 40 wt-percent NaCl solution. Geochim. Cosmochim. Acta 58, 1053–1063.

Bruckschen, P., Oesmann, S., Veizer, J., 1999. Isotope stratigraphy of the European Carboniferous: proxy signals for ocean chemistry, climate and tectonics. Chem. Geol. 161, 127–163.

Burke, W., Denison, R., Hetherington, E., Koepnick, R., Nelson, H., Otto, J., 1982. Variation of seawater $^{87}Sr/^{86}Sr$ throughout Phanerozoic time. Geology 10, 516–519.

Chen, C.M., Lu, H.F., Jia, D., Cai, D.S., Wu, S.M., 1999. Closing history of the southern Tianshan oceanic basin, western China: an oblique collisional orogeny. Tectonophysics 302, 23–40.

Chen, H.Y., Kyser, T.K., Clark, A.H., 2011. Contrasting fluids and reservoirs in the contiguous Marcona and Mina Justa iron oxide-Cu (-Ag-Au) deposits, south-central Peru. Mineral. Deposita 46, 677–706.

Debruyne, D., Hulsbosch, N., Muchez, P., 2016. Unraveling rare earth element signatures in hydrothermal carbonate minerals using a source-sink system. Ore Geol. Rev. 72, 232–252.

Deng, J., Liu, X., Wang, Q., Pan, R., 2015. Origin of the Jiaodong-type Xinli gold deposit, Jiaodong Peninsula, China: constraints from fluid inclusion and C-D-O-S-Sr isotope compositions. Ore Geol. Rev. 65, 674–686.

Dill, H.G., 2010. The "chessboard" classification scheme of mineral deposits: mineralogy and geology from aluminum to zirconium. Earth Sci. Rev. 100, 1–420.

Duan, S., Zhang, Z., Jiang, Z., Zhao, J., Zhang, Y., Li, F., Tian, J., 2014. Geology, geochemistry, and geochronology of the Dunde iron–zinc ore deposit in western Tianshan, China. Ore Geol. Rev. 57, 441–461.

Feng, J.X., Shi, F.P., Wang, B.Y., Hu, J.M., Wang, J.T., Tian, J.Q., 2010. Volcanogenic Iron Deposits in the Awulale Metallogenic Belt in Western Tianshan. Geological Publishing House, Beijing, pp. 16–112.

Gao, J., Long, L., Klemd, R., Qian, Q., Liu, D., Xiong, X., Su, W., Liu, W., Wang, Y., Yang, F., 2009a. Tectonic evolution of the south Tianshan orogen and adjacent regions, NW China: geochemical and age constraints of granitoid rocks. Int. J. Earth Sci. 98, 1221–1238.

Gao, J., Qian, Q., Long, L.L., Zhang, X., Li, J.L., Su, W., 2009b. Accretionary orogenic process of western Tianshan, China. Geol. Bull. China 28, 1804–1816.

Gao, J., Li, M.S., Xiao, X.C., Tang, Y.Q., He, G.Q., 1998. Paleozoic tectonic evolution of the Tianshan orogen, northwestern China. Tectonophysics 287, 213–231.

Ge, S., Du, Y., Wang, S., Li, D., Pang, Z., Shen, L., Wang, K., Jin, X., 2014. Genesis of skarn from Dunde iron deposit in western Tianshan, Xinjiang: mineralogical and REE constraints. Geoscience 28, 61–72.

Ge, S.S., 2013. Characteristics and Genesis of the Dunde Iron Deposit in Xinjiang Province Master Thesis, 28.

Grant, J.A., 1986. The isocon diagram –– a simple solution to Gresens equation for metasomatic alteration. Econ. Geol. 81, 1976–1982.

Hecht, L., Freiberger, R., Gilg, H.A., Grundmann, G., Kostitsyn, Y.A., 1999. Rare earth element and isotope (C, O, Sr) characteristics of hydrothermal carbonates: genetic implications for dolomite-hosted talc mineralization at Göpfersgrün (Fichtelgebirge, Germany). Chem. Geol. 155, 115–130.

Henderson, P., 1984. Chapter 1 – general geochemical properties and abundances of the rare earth elements. Dev. Geochem., 1–32

Hoefs, J., 1997. Stable Isotope Geochemistry. Springer, Berlin, pp. 65–168.

Hong, W., Zhang, Z.H., Zhao, J., Wang, Z.H., Li, F.M., Shi, F.P., Liu, X.Z., 2012. Mineralogy of the Chagangnuoer iron deposit in western Tianshan Mountains, Xinjiang, and its geological significance. Acta Petrol. Mineral. 31, 191–211 (in Chinese with English abstract).

Hou, T., Zhang, Z., Pirajno, F., Santosh, M., Encarnacion, J., Liu, J., Zhao, Z., Zhang, L., 2014a. Geology, tectonic settings and iron ore metallogenesis associated with submarine volcanism in China: an overview. Ore Geol. Rev. 57, 498–517.

Hou, T., Zhang, Z., Santosh, M., Encarnacion, J., Zhu, J., Luo, W., 2014b. Geochronology and geochemistry of submarine volcanic rocks in the Yamansu iron deposit, eastern Tianshan Mountains, NW China: constraints on the metallogenesis. Ore Geol. Rev. 56, 487–502.

Hu, A., Jahn, B.-M., Zhang, G., Chen, Y., Zhang, Q., 2000. Crustal evolution and Phanerozoic crustal growth in northern Xinjiang: Nd isotopic evidence. Part I. Isotopic characterization of basement rocks. Tectonophysics 328, 15–51.

Hu, R.-Z., Liu, J.-M., Zhai, M.-G. (Eds.), 2011. Mineral Resources Science in China: A Roadmap to 2050. Science Press, Springer, Beijing (93 pp.).

Jiang, F.Z., Wang, Y.W., 2005. Marine Volcanic Rocks and Related Metallic Ore Deposits. Metallurgical Industry Press, Beijing (in Chinese).

Jiang, Z.S., Zhang, Z.H., Wang, Z.H., Duan, S.G., Li, F.M., Tian, J.Q., 2014. Geology, geochemistry, and geochronology of the Zhibo iron deposit in the western Tianshan, NW China: constraints on metallogenesis and tectonic setting. Ore Geol. Rev. 57, 406–424.

Kontak, D.J., Kerrich, R., 1997. An isotopic (C, O, Sr) study of vein gold deposits in the Meguma terrane, Nova Scotia; implication for source reservoirs. Econ. Geol. 92, 161–180.

Lecumberri-Sanchez, P., Steele-MacInnis, M., Bodnar, R.J., 2012. A numerical model to estimate trapping conditions of fluid inclusions that homogenize by halite disappearance. Geochim. Cosmochim. Acta 92, 14–22.

Lecumberri-Sanchez, P., Steele-MacInnis, M., Weis, P., Driesner, T., Bodnar, R.J., 2015. Salt precipitation in magmatic-hydrothermal systems associated with upper crustal plutons. Geology 43, 1063–1066.

Li, G., Sizaret, S., Branquet, Y., Barbanson, L., Chen, Y., Wang, B., Wu, C., Gu, L., Shu, L., 2014. Initial geometry and paleoflow reconstruction of the Yamansu skarn-related iron deposit of eastern Tianshan (China) from paleomagnetic and magnetic fabrics investigations. J. Asian Earth Sci. 93, 1–14.

Li, H.-M., Li, L.-X., Yang, X.-Q., Cheng, Y.-B., 2015a. Types and geological characteristics of iron deposits in China. J. Asian Earth Sci. 103, 2–22.

Li, N.-B., Niu, H.-C., Zhang, X.-C., Zeng, Q.-S., Shan, Q., Li, C.-Y., Yan, S., Yang, W.-B., 2015b. Age, petrogenesis and tectonic significance of the ferrobasalts in the Chagangnuoer iron deposit, western Tianshan. Int. Geol. Rev. 57, 1218–1238.
Li, J.L., Su, W., Zhang, X., 2009a. Zircon Cameca U-Pb dating and its significance for granulite-facies granitic gneisses from the west Awulale Mountains, west Tianshan. Geol. Bull. Chin. 28, 1852–1862.
Li, Y.J., Li, Z.C., Zhou, J.B., Gao, Z.H., Gao, Y.L., Tong, L.M., Liu, J., 2009b. Division of the Carboniferous lithostratigraphic units in Awulale area, western Tianshan. Acta Petrol. Sin. 25, 1332–1340.
Li, X.-H., 1997. Geochemistry of the Longsheng ophiolite from the southern margin of Yangtze Craton, SE China. Geochem. J. 31, 323–338.
Liu, H., Wang, B., Shu, L., Jahn, B.-M., Lizuka, Y., 2014. Detrital zircon ages of Proterozoic meta-sedimentary rocks and Paleozoic sedimentary cover of the northern Yili block: implications for the tectonics of microcontinents in the Central Asian Orogenic Belt. Precambrian Res. 252, 209–222.
Liu, X.-J., Liu, W., Liu, L.-J., 2012. The generation of a stratiform skarn and volcanic exhalative Pb–Zn deposit (Sawusi) in the southern Chinese Altay Mountains: the constraints from petrography, mineral assemblage and chemistry. Gondwana Res. 22, 597–614.
Meinert, L.D., Dipple, G.M., Nicolescu, S., 2005. World Skarn Deposits, Economic Geology 100th Anniversary Volume, pp. 299–336.
Muchez, P., Corbella, M., 2012. Factors controlling the precipitation of copper and cobalt minerals in sediment-hosted ore deposits: advances and restrictions. J. Geochem. Explor. 118, 38–46.
Munemoto, T., Ohmori, K., Iwatsuki, T., 2015. Rare earth elements (REE) in deep groundwater from granite and fracture-filling calcite in the Tono area, central Japan: prediction of REE fractionation in paleo- to present-day groundwater. Chem. Geol. 417, 58–67.
Ohmoto, H., 1972. Systematics of sulfur and carbon isotopes in hydrothermal ore deposits. Econ. Geol. 67 (551-&).
Peng, J.T., Hu, R.Z., 2001. Metallogenic epoch and metallogenic tectonic environment of antimony deposits, South China. Geol. Geochem. 29, 104–108 (in Chinese).
Pokrovsky, B.G., Bujakaite, M.I., 2015. Geochemistry of C, O, and Sr isotopes in the Neoproterozoic carbonates from the southwestern Patom paleobasin, southern middle Siberia. Lithol. Miner. Resour. 50, 144–169.
Richards, J.P., 2015. The oxidation state, and sulfur and Cu contents of arc magmas: implications for metallogeny. Lithos 233, 27–45.
Sengör, A.M.C., Natalin, B.A., Burtman, V.S., 1993. Evolution of the Altaid tectonic collage and Paleozoic crustal growth in Eurasia. Nature 364, 299–307.
Shannon, R., 1976. Revised effective ionic radii and systematic studies of interatomic distances in halides and chalcogenides. Acta Crystallogr. A 32, 751–767.
Shen, N.P., Peng, J.T., Hu, R.Z., Liu, S., Coulson, I.M., 2011. Strontium and lead isotopic study of the carbonate-hosted Xujiashan antimony deposit from Hubei Province, South China: implications for its origin. Resour. Geol. 61, 52–62.
Sheppard, S.M.F., 1986. Characterization and isotopic variations in natural waters. Rev. Mineral. 16, 165–183.
Sun, S.-S., McDonough, W.F., 1989. Chemical and isotopic systematics of oceanic basalts: implications for mantle composition and processes. Geol. Soc. Lond., Spec. Publ. 42, 313–345.
Sun, W.L., Niu, Y.L., Ma, Y.X., Liu, Y., Zhang, G.R., Hu, Z.X., Zhang, Z.W., Chen, S., Li, J. Y., Wang, X.H., Gong, H.M., 2015. Petrogenesis of the Chagangnuoer deposit, NW China: a general model for submarine volcanic-hosted skarn iron deposits. Sci. Bull. 60, 363–379.
Sverjensky, D.A., 1984. Europium redox equilibria in aqueous-solution. Earth Planet. Sci. Lett. 67, 70–78.
Tanaka, K., Kawabe, I., 2006. REE abundances in ancient seawater inferred from marine limestone and experimental REE partition coefficients between calcite and aqueous solution. Geochem. J. 40, 425–435.
Tanaka, K., Takahashi, Y., Shimizu, H., 2008. Local structure of Y and Ho in calcite and its relevance to Y fractionation from Ho in partitioning between calcite and aqueous solution. Chem. Geol. 248, 104–113.
Tang, G.-J., Chung, S.-L., Wang, Q., Wyman, D.A., Dan, W., Chen, H.-Y., Zhao, Z.-H., 2014. Petrogenesis of a Late Carboniferous mafic dike–granitoid association in the western Tianshan: response to the geodynamics of oceanic subduction. Lithos 202–203, 85–99.
Taylor, S.R., McLennan, S.M., 1988. The significance of the rare earths in geochemistry and cosmochemistry. In: Handbook on the Physics and Chemistry of Rare Earths. Elsevier, pp. 485–578. Chapter 79.
Torresi, I., Xavier, R.P., Bortholoto, D.F.A., Monteiro, L.V.S., 2012. Hydrothermal alteration, fluid inclusions and stable isotope systematics of the Alvo 118 iron oxide-copper-gold deposit, Carajas Mineral Province (Brazil): implications for ore genesis. Mineral. Deposita 47, 299–323.
Uysal, I.T., Zhao, J.X., Golding, S.D., Lawrence, M.G., Glikson, M., Collerson, K.D., 2007. Sm-Nd dating and rare-earth element tracing of calcite: implications for fluid-flow events in the Bowen Basin, Australia. Chem. Geol. 238, 63–71.
Veizer, J., 1989. Strontium isotopes in seawater through time. Annu. Rev. Earth Planet. Sci. 17, 141–167.
Veizer, J., Hoefs, J., 1976. Nature of O18–O16 and C13–C12 secular trends in sedimentary carbonate rocks. Geochim. Cosmochim. Acta 40, 1387–1395.
Veizer, J., Ala, D., Azmy, K., Bruckschen, P., Buhl, D., Bruhn, F., Carden, G.A.F., Diener, A., Ebneth, S., Godderis, Y., Jasper, T., Korte, C., Pawellek, F., Podlaha, O.G., Strauss, H., 1999. Sr-87/Sr-86, delta C-13 and delta O-18 evolution of Phanerozoic seawater. Chem. Geol. 161, 59–88.
Veizer, J., Buhl, D., Diener, A., Ebneth, S., Podlaha, O.G., Bruckschen, P., Jasper, T., Korte, C., Schaaf, M., Ala, D., Azmy, K., 1997. Strontium isotope stratigraphy: potential resolution and event correlation. Palaeogeogr. Palaeoclimatol. Palaeoecol. 132, 65–77.
Wang, B., Faure, M., Shu, L.S., Cluzel, D., Charvet, J., De Jong, K., Chen, Y., 2008. Paleozoic tectonic evolution of the Yili Block, western Chinese Tianshan. Bull. Soc. Geol. Fr. 179, 483–490.
Wang, B., Liu, H., Shu, L., Jahn, B.-M., Chung, S.-L., Zhai, Y., Liu, D., 2014b. Early Neoproterozoic crustal evolution in northern Yili Block: insights from migmatite, orthogneiss and leucogranite of the Wenquan metamorphic complex in the NW Chinese Tianshan. Precambrian Res. 242, 58–81.
Wang, B., Shu, L.S., Cluzel, D., Faure, M., Charvet, J., 2007. Geochemical constraints on carboniferous volcanic rocks of the Yili Block (Xinjiang, NW China): implication for the tectonic evolution of western Tianshan. J. Asian Earth Sci. 29, 148–159.
Wang, B.Y., Hu, X.J., Wang, J.T., Shao, Q.H., Ling, J.L., Gou, N.X., Zhao, Y.F., Xia, Z.D., Jiang, C.Y., 2011. Geological characteristics and genesis of Chagannur iron deposit in western Tianshan, Xinjiang. Mineral Deposits 30, 385–402.
Wang, J., Wen, H., Fan, H., Zhu, J., 2012. Sm-Nd geochronology, REE geochemistry and C and O isotope characteristics of calcites and stibnites from the Banian antimony deposit, Guizhou Province, China. Geochem. J. 46, 393–407.
Wang, Q., Lin, Z., Huang, C., Huang, Q., Zhen, J., 2001. Metallogenic series and prospecting target of ore deposits at Chagangnur region of the western Tianshan. Xinjiang Geol. 19, 263–267 (in Chinese).
Wang, S., Magalhaes, V.H., Pinheiro, L.M., Liu, J., Yan, W., 2015. Tracing the composition, fluid source and formation conditions of the methane-derived authigenic carbonates in the Gulf of Cadiz with rare earth elements and stable isotopes. Mar. Pet. Geol. 68, 192–205.
Wang, Z., Wu, J., Lu, X., Liu, C., Zhang, J., 1990. Polycyclic Tectonic Evolution and Metallogeny of the Tianshan Mountains (in Chinese), 29. Science Press, Beijing, p. 37.
Webb, G.E., Kamber, B.S., 2000. Rare earth elements in Holocene reefal microbialites: a new shallow seawater proxy. Geochim. Cosmochim. Acta 64, 1557–1565.
Webster, J.D., 1997. Exsolution of magmatic volatile phases from Cl-enriched mineralizing granitic magmas and implications for ore metal transport. Geochim. Cosmochim. Acta 61, 1017–1029.
Webster, J.D., Kinzler, R.J., Mathez, E.A., 1999. Chloride and water solubility in basalt and andesite melts and implications for magmatic degassing. Geochim. Cosmochim. Acta 63, 729–738.
Wen, H., Chen, H., Wen, L., Zhou, G., Feng, Q., Li, S., 2014. Diagenetic fluids of paleokarst reservoirs in Carboniferous from eastern Sichuan Basin: some evidences from fluid inclusion, trace element and C-O-Sr isotope. Acta Petrol. Sin. 30, 655–666.
Xavier, R.P., Wiedenbeck, M., Trumbull, R.B., Dreher, A.M., Monteiro, L.V.S., Rhede, D., de Araujo, C.E.G., Torresi, I., 2008. Tourmaline B-isotopes fingerprint marine evaporites as the source of high-salinity ore fluids in iron oxide copper-gold deposits, Carajas Mineral Province (Brazil). Geology 36, 743–746.
Xiao, W.J., Windley, B.F., Allen, M.B., Han, C.M., 2013. Paleozoic multiple accretionary and collisional tectonics of the Chinese Tianshan orogenic collage. Gondwana Res. 23, 1316–1341.
Xu, L.G., Mao, J.W., Yang, F.Q., Hennig, D., Zheng, J.M., 2010. Geology, geochemistry and age constraints on the Mengku skarn iron deposit in Xinjiang Altai, NW China. J. Asian Earth Sci. 39, 423–440.
Yan, S., Shan, Q., Niu, H.-C., Yang, W.-B., Li, N.-B., Zeng, L.-J., Jiang, Y.-H., 2015. Petrology and geochemistry of Late Carboniferous hornblende gabbro from the Awulale Mountains, western Tianshan (NW China): implication for an arc–nascent back-arc environment. J. Asian Earth Sci. 113 (Part 1), 218–237.
Yang, W.-B., Niu, H.-C., Shan, Q., Chen, H.-Y., Hollings, P., Li, N.-B., Yan, S., Zartman, R. E., 2014. Geochemistry of primary-carbonate bearing K-rich igneous rocks in the Awulale Mountains, western Tianshan: implications for carbon-recycling in subduction zone. Geochim. Cosmochim. Acta 143, 143–164.
Yang, W.-B., Niu, H.-C., Shan, Q., Luo, Y., Sun, W.-D., Li, C.-Y., Li, N.-B., Yu, X.-Y., 2012. Late Paleozoic calc-alkaline to shoshonitic magmatism and its geodynamic implications, Yuximolegai area, western Tianshan, Xinjiang. Gondwana Res. 22, 325–340.
Yuan, T., 2003. Contrast of geological characteristics between Motuoshala iron (manganese) deposit and Shikebutai iron deposit in west Tianshan Mountain of Xinjiang Autonomous Region. Contrib. Geol. Miner. Resour. Res. 18, 88–92 (in Chinese).
Zaky, A.H., Brand, U., Azmy, K., 2015. A new sample processing protocol for procuring seawater REE signatures in biogenic and abiogenic carbonates. Chem. Geol. 416, 36–50.
Zhang, X., Tian, J.Q., Gao, J., Klemd, R., Dong, L.H., Fan, J.J., Jiang, T., Hu, C.J., Qian, Q., 2012a. Geochronology and geochemistry of granitoid rocks from the Zhibo syngenetic volcanogenic iron ore deposit in the western Tianshan Mountains (NW-China): constraints on the age of mineralization and tectonic setting. Gondwana Res. 22, 585–596.
Zhang, Z., Hong, W., Jiang, Z., Duan, S., Xu, L., Li, F., Guo, X., Zhao, Z., 2012b. Geological characteristics and zircon U-Pb dating of volcanic rocks from the Beizhan iron deposit in western Tianshan Mountains, Xinjiang, NW China. Acta Geograph. Sin. 86, 737–747 (Engl).
Zhang, Z., Hou, T., Santosh, M., Li, H., Li, J., Zhang, Z., Song, X., Wang, M., 2014. Spatio-temporal distribution and tectonic settings of the major iron deposits in China: an overview. Ore Geol. Rev. 57, 247–263.

Zhao, X.F., Zhou, M.F., 2011. Fe–Cu deposits in the Kangdian region, SW China: a Proterozoic IOCG (iron-oxide–copper–gold) metallogenic province. Mineral. Deposita 46, 731–747.

Zheng, Y.F., 1990. Carbon-oxygen isotopic covariation in hydrothermal calcite during degassing of CO_2 - a quantitative-evaluation and application to the Kushikino gold mining area in Japan. Mineral. Deposita 25, 246–250.

Zheng, Y.F., 1999. Oxygen isotope fractionation in carbonate and sulfate minerals. Geochem. J. 33, 109–126.

Zheng, Y.F., Hoefs, J., 1993. Carbon and oxygen isotopic covariations in hydrothermal calcites-theoretical modeling on mixing processes and application to Pb-Zn deposits in the Harz Mountains, Germany. Mineral. Deposita 28, 79–89.

Zhong, S., Mucci, A., 1995. Partitioning of rare earth elements (REE) between calcite and seawater solutions at 25 °C and 1 atm, and high dissolved REE concentrations. Geochim. Cosmochim. Acta 59, 443–453.

Zhu, Y., Guo, X., Song, B., Zhang, L., Gu, L., 2009. Petrology, Sr–Nd–Hf isotopic geochemistry and zircon chronology of the Late Palaeozoic volcanic rocks in the southwestern Tianshan Mountains, Xinjiang, NW China. J. Geol. Soc. 166, 1085–1099.

Zhu, Y.F., Zhou, J., Guo, X., 2006. Petrology and Sr-Nd isotopic geochemistry of the Carboniferous volcanic rocks in the western Tianshan Mountains, NW China. Acta Petrol. Sin. 22, 1341–1350.

View publication stats